Title

Molecular anatomy of adult mouse leptomeninges

Journal

Neuron, 111(23)

ISSN

0896-6273

Authors

Pietilä, Riikka
Del Gaudio, Francesca
He, Liqun
et al.

Publication Date

2023-12-01

DOI

10.1016/j.neuron.2023.09.002

Neuron

NeuroResource

Molecular anatomy of adult mouse leptomeninges

Graphical abstract

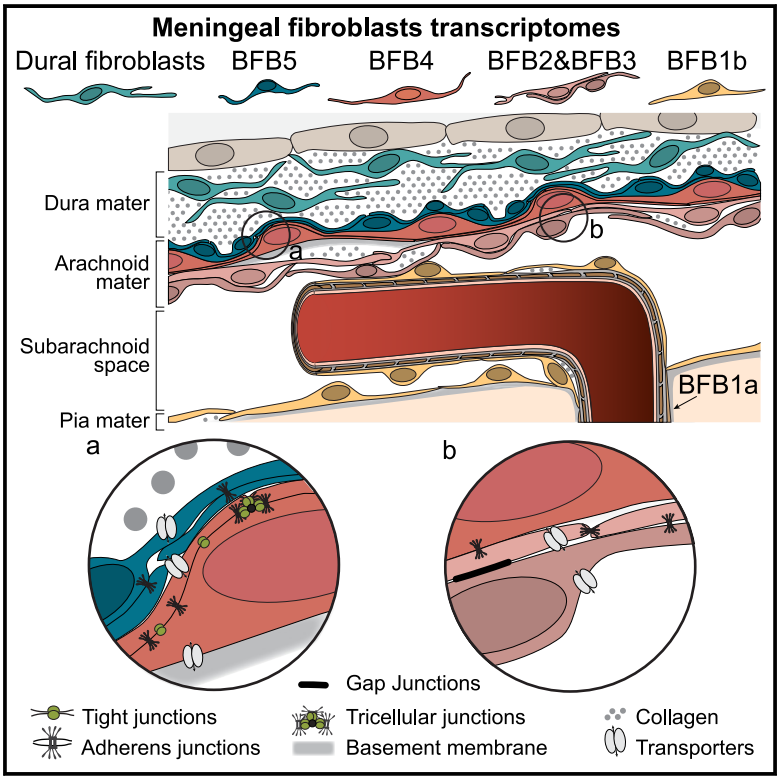

Highlights

- The brain has six transcriptionally distinguishable fibroblast subtypes: BFB1–6
- Five BFB subtypes form the pial and arachnoid layers of the leptomeninges
- Demonstration of multicellular and junctional nature of the arachnoid barrier layer
- Utility of BFB markers in meningeal research, spanning development to disease

Authors

Riikka Pietilä, Francesca Del Gaudio, Liqun He, ..., Urban Lendahl, Johanna Andrae, Christer Betsholtz

Correspondence

christer.betsholtz@igp.uu.se

In brief

This study establishes the molecular and anatomical landscape of mouse brain fibroblasts using single-cell transcriptomics and *in situ* RNA-, protein-, and reporter-labeling, specifically focusing on the leptomeninges. The data pave the way for further studies of brain fibroblasts and their role in CNS barrier functions in health and disease.

Pietilä et al., 2023, Neuron *111*, 1–20
December 6, 2023
https://doi.org/10.1016/j.neuron.2023.09.002

CellPress

Neuron

CellPress
OPEN ACCESS

NeuroResource

Molecular anatomy of adult mouse leptomeninges

Riikka Pietilä,[1,17] Francesca Del Gaudio,[2,3,17] Liqun He,[1,17] Elisa Vázquez-Liébanas,[1,17] Michael Vanlandewijck,[1,2] Lars Muhl,[2] Giuseppe Mocci,[2] Katrine D. Bjørnholm,[4] Caroline Lindblad,[5,6,7] Alexander Fletcher-Sandersjöö,[5,8] Mikael Svensson,[5,9] Eric P. Thelin,[5,9] Jianping Liu,[2] A. Jantine van Voorden,[1,18] Monica Torres,[1,19] Salli Antila,[10] Li Xin,[11] Helena Karlström,[4] Jon Storm-Mathisen,[12] Linda Hildegard Bergersen,[13,14] Aldo Moggio,[3,20] Emil M. Hansson,[3] Maria H. Ulvmar,[15] Per Nilsson,[4] Taija Mäkinen,[1] Maarja Andaloussi Mäe,[1] Kari Alitalo,[10] Steven T. Proulx,[11] Britta Engelhardt,[11] Donald M. McDonald,[16] Urban Lendahl,[3,17] Johanna Andrae,[1,17,21] and Christer Betsholtz[1,2,17,22,*]

[1]Department of Immunology, Genetics and Pathology, Rudbeck Laboratory, Uppsala University, 75185 Uppsala, Sweden
[2]Department of Medicine Huddinge, Karolinska Institutet, 14157 Huddinge, Sweden
[3]Department of Cell and Molecular Biology, Karolinska Institutet, 17177 Stockholm, Sweden
[4]Department of Neurobiology, Care Sciences and Society, Division of Neurogeriatrics, Center for Alzheimer Research, Karolinska Institutet, 17177 Stockholm, Sweden
[5]Department of Clinical Neuroscience, Karolinska Institutet, 17177 Stockholm, Sweden
[6]Department of Neurosurgery, Uppsala University Hospital, 75185 Uppsala, Sweden
[7]Department of Medical Sciences, Uppsala University, 75185 Uppsala, Sweden
[8]Department of Neurosurgery, Karolinska University Hospital, 17176 Stockholm, Sweden
[9]Department of Neurology, Karolinska University Hospital, 17176 Stockholm, Sweden
[10]Wihuri Research Institute and Translational Cancer Medicine Program, University of Helsinki, 00014 Helsinki, Finland
[11]Theodor Kocher Institute, University of Bern, 3012 Bern, Switzerland
[12]Division of Anatomy, Department of Molecular Medicine, Institute of Basic Medical Sciences, University of Oslo, 0317 Oslo, Norway
[13]Brain and Muscle Energy Group, Institute of Oral Biology, University of Oslo, 0316 Oslo, Norway
[14]Center for Healthy Aging, Copenhagen University, 2200 Copenhagen, Denmark
[15]Department of Medical Biochemistry and Microbiology, Uppsala University, 75123 Uppsala, Sweden
[16]Cardiovascular Research Institute, UCSF Helen Diller Family Comprehensive Cancer Center, and Department of Anatomy, University of California, San Francisco, San Francisco, CA 94143, USA
[17]These authors contributed equally
[18]Present address: Reproductive Biology Laboratory, Amsterdam University Medical Centers, Amsterdam, the Netherlands
[19]Present address: Dermatology and Venerology Division, Department of Medicine Solna, Karolinska Institutet, 17176 Stockholm, Sweden
[20]Present address: Department of Cardiology, German Heart Centre Munich, Technical University Munich, 80333 Munich, Germany
[21]Present address: The Swedish Childhood Cancer Fund, 10368 Stockholm, Sweden
[22]Lead contact
*Correspondence: christer.betsholtz@igp.uu.se
https://doi.org/10.1016/j.neuron.2023.09.002

SUMMARY

Leptomeninges, consisting of the pia mater and arachnoid, form a connective tissue investment and barrier enclosure of the brain. The exact nature of leptomeningeal cells has long been debated. In this study, we identify five molecularly distinct fibroblast-like transcriptomes in cerebral leptomeninges; link them to anatomically distinct cell types of the pia, inner arachnoid, outer arachnoid barrier, and dural border layer; and contrast them to a sixth fibroblast-like transcriptome present in the choroid plexus and median eminence. Newly identified transcriptional markers enabled molecular characterization of cell types responsible for adherence of arachnoid layers to one another and for the arachnoid barrier. These markers also proved useful in identifying the molecular features of leptomeningeal development, injury, and repair that were preserved or changed after traumatic brain injury. Together, the findings highlight the value of identifying fibroblast transcriptional subsets and their cellular locations toward advancing the understanding of leptomeningeal physiology and pathology.

INTRODUCTION

The adult central nervous system (CNS) is shielded from surrounding tissues by cellular barriers that prevent the uncontrolled exchange of molecules. In mammals, these barriers are formed by distinct cell types: meningeal cells/fibroblasts (FBs), glia limitans astrocytes, blood vessel endothelial cells (ECs), choroid plexus epithelial cells, and circumventricular organ ependymal (Epend) cells.[1,2] The cranial meninges consist of membranes located between the brain and skull that are conventionally divided into three layers: the delicate innermost pia mater that lines the brain surface, the middle arachnoid, and the fibrous outermost dura mater next to the skull. The arachnoid and pia, collectively called leptomeninges[3] (Figure 1A), are separated

Please cite this article in press as: Pietilä et al., Molecular anatomy of adult mouse leptomeninges, Neuron (2023), https://doi.org/10.1016/j.neuron.2023.09.002

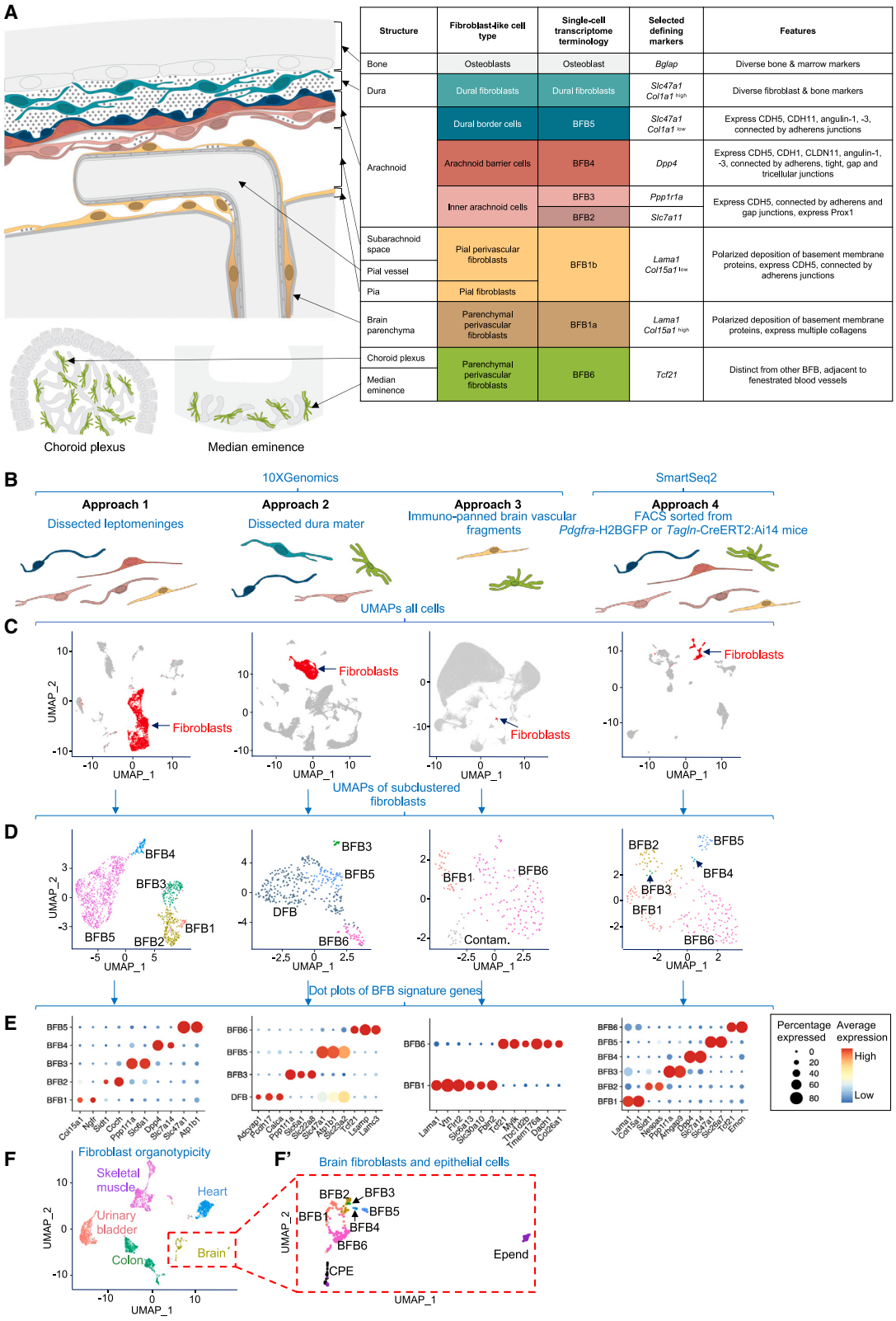

Structure	Fibroblast-like cell type	Single-cell transcriptome terminology	Selected defining markers	Features
Bone	Osteoblasts	Osteoblast	*Bglap*	Diverse bone & marrow markers
Dura	Dural fibroblasts	Dural fibroblasts	*Slc47a1* *Col1a1* high	Diverse fibroblast & bone markers
Arachnoid	Dural border cells	BFB5	*Slc47a1* *Col1a1* low	Express CDH5, CDH11, angulin-1, -3, connected by adherens junctions
	Arachnoid barrier cells	BFB4	*Dpp4*	Express CDH5, CDH1, CLDN11, angulin-1, -3, connected by adherens, tight, gap and tricellular junctions
	Inner arachnoid cells	BFB3	*Ppp1r1a*	Express CDH5, connected by adherens and gap junctions, express Prox1
		BFB2	*Slc7a11*	
Subarachnoid space	Pial perivascular fibroblasts	BFB1b	*Lama1* *Col15a1* low	Polarized deposition of basement membrane proteins, express CDH5, connected by adherens junctions
Pial vessel				
Pia	Pial fibroblasts			
Brain parenchyma	Parenchymal perivascular fibroblasts	BFB1a	*Lama1* *Col15a1* high	Polarized deposition of basement membrane proteins, express multiple collagens
Choroid plexus	Parenchymal perivascular fibroblasts	BFB6	*Tcf21*	Distinct from other BFB, adjacent to fenestrated blood vessels
Median eminence				

(legend on next page)

Please cite this article in press as: Pietilä et al., Molecular anatomy of adult mouse leptomeninges, Neuron (2023), https://doi.org/10.1016/j.neuron.2023.09.002

by the subarachnoid space (SAS), which contains cerebrospinal fluid (CSF), arteries, and veins, but not capillaries.

The brain, blood, and CSF compartments are separated by three cellular barriers: the arachnoid barrier (AB), which separates CSF in the SAS from interstitial fluid in the dura and beyond; the blood-brain barrier (BBB), which separates blood from interstitial fluid in the CNS; and the blood-CSF barrier, which separates interstitial fluid in the choroid plexus from CSF in cerebral ventricles.[4–6] The choroid plexus, as a major source of CSF,[7,8] consists of a layer of epithelial cells overlying a core of fenestrated blood vessels and stromal cells.[9]

Unlike CNS ECs of the BBB and choroid plexus epithelial cells of the blood-CSF barrier,[10–12] cells that form the AB are poorly characterized. Tight intercellular junctions are a unifying feature of all barrier-forming cells. Yet, it is unclear how tight junctions and barrier functions are distributed among the cells of the leptomeninges. Pial FBs, AB cells (ABCs), and dural border cells have been anatomically defined,[13] but many features of these cells are still unknown. Studies of brain and meningeal development[14,15] suggest that ABCs differentiate from head mesenchyme, implicating a FB-like origin, whereas their expression of E-cadherin[16–18] is similar to epithelial cells. Mesothelial characteristics of arachnoid cells have also been described,[19] and dural border cells have been called neurothelial cells.[20,21] FB-like cells (FL) have been described in the arachnoid and the pia[13,22–24] and around blood vessels in the spinal cord and brain.[25–30] FBs are also abundant around choroid plexus blood vessels.[31,32]

Brain FBs (BFBs) are implicated in physiological and pathological processes,[3,30] where expression of fibrosis-related genes increases in encephalitis[33] and fibrotic scars in the brain and spinal cord.[26,34,35] FB activation has also been implicated in the pathogenesis of amyotrophic lateral sclerosis,[36] stroke,[37,38] and traumatic brain injury (TBI),[39] but other cell types could also be involved.[40–42]

To develop a more complete understanding of the molecular features of FBs in and around the brain, we mapped brain and meningeal FB heterogeneity using single-cell RNA sequencing (scRNA-seq), revealing six distinct FB subtypes distributed among the leptomeningeal layers, pial blood vessels, choroid plexus, and median eminence (Figure 1A).

RESULTS

Single-cell transcriptomic analysis reveals six brain and leptomeningeal FB types: BFB1–6

Scarcity of BFBs has made it difficult to obtain sufficient numbers for comprehensive scRNA-seq analysis in whole brain[29,43] or brain vasculature.[28] Accordingly, we used four complementary approaches for cell capture and scRNA-seq analysis of FB subtypes in the leptomeninges and parts of the brain. Cells were dissected from leptomeninges or dura mater or were obtained from microvascular fragments and fluorescence-activated cell sorting (FACS) from two reporter mouse strains (see Figures 1B and S1–S4 and STAR Methods). We also re-analyzed relevant previously published scRNA-seq data[28,44] (Figures S5 and S6) and compared the different datasets, keeping separate the data from different scRNA-seq techniques and batches in searchable databases (see links in Figures S1–S6).

From the leptomeninges, 4,862 single-cell transcriptomes were obtained, including 1,341 presumptive FB transcriptomes, as judged by the abundance of collagen (*Col)1a1* (type 1 alpha 1 chain), *Col1a2*, and *Dcn* (decorin) transcripts and lack of canonical markers of immune cells (e.g., *Ptprc* [protein tyrosine phosphatase receptor type C]), astrocytes (e.g., *Gfap* [glial fibrillary acidic protein]), oligodendrocytes (e.g., *Mbp* [myelin basic protein]), ECs (e.g., *Pecam1* [platelet and endothelial cell adhesion molecule 1]), and mural cells (e.g., *Myh11* [myosin heavy chain 11]) (Figures 1C and S1). The dural dissection yielded 28,352 single-cell transcriptomes, including 4,061 transcriptomes interpreted as FBs by the same criteria (Figures 1C and S2). Dural FBs also included a small cluster of osteoblasts (e.g., *Bglap* [osteocalcin] and *Sparc* [osteonectin]), presumably from the skull inner surface (Figure S2A). Among the 272,443 vascular and glial single-cell transcriptomes from vascular fragments, we identified 173 FB transcriptomes (Figures 1C and S3). Cells sorted from *Pdgfra* (platelet-derived growth factor receptor alpha)-H2BGFP[45] and *Tagln* (transgelin)-CreERT2:Ai14[46,47] mice yielded 234 FB transcriptomes, again among a majority derived from other vascular and glial cells (Figures 1C and S4).

FB heterogeneity was examined by sub-clustering of FB populations from each approach and mapping subclusters by uniform manifold approximation and projection (UMAP) projections, gene expression heatmaps, dot plots, and bar plots (for details, see Figures S1–S4 and STAR Methods). Common FB subtypes in the datasets were identified by using FB-subtype-specific marker vignettes (for details, see Figures 1D, 1E, S1, and S2) as a guide for cross-comparison. This approach revealed six distinct groups of brain and leptomeningeal FB transcriptomes, referred to as BFB1–6.

Each BFB transcriptome was characterized by a unique combination of markers (for overview, see Figures 1A and 1E; for further details; see Figures 3, 4, 5, and S1). Briefly, BFB1 transcriptomes were enriched in *Col15a1*, *Lama1* (laminin-alpha 1), and *Fbln2* (fibulin 2) and expressed high levels of *Lamb1*, *Lamc1*, *Col4a1*, *Col4a2*, and *Col4a5*, consistent with basement

Figure 1. Brain fibroblast isolation, single-cell RNA sequencing, sub-clustering, and annotation

(A) Schematic illustration of the brain regions examined (meninges, blood vessels, choroid plexus, and median eminence) and table summarizing the locations and features of BFB1–6.

(B) Outline of the four approaches used to generate single-cell suspensions and scRNA-seq methodologies.

(C) UMAP visualization of all single-cell transcriptomes and identification of fibroblast cluster(s) (red).

(D) UMAP plots of subclustered fibroblasts and annotation of BFB1–6 fibroblast transcriptome subtypes.

(E) Dot plots of selected signature markers used to identify BFB1–6 and to generate tools for *in situ* expression analyses.

(F) UMAP of the SmartSeq2 transcriptomes of fibroblasts and selected epithelial cells from mouse brain, heart, skeletal muscle, colon, and urinary bladder.

(F′) UMAP of SmartSeq2 transcriptomes for BFB1–6 and ependymal and choroid plexus epithelial cells.

BFB, brain fibroblast; FB, fibroblast; CPE, choroid plexus epithelium; Epend, ependymal cells.

Please cite this article in press as: Pietilä et al., Molecular anatomy of adult mouse leptomeninges, Neuron (2023), https://doi.org/10.1016/j.neuron.2023.09.002

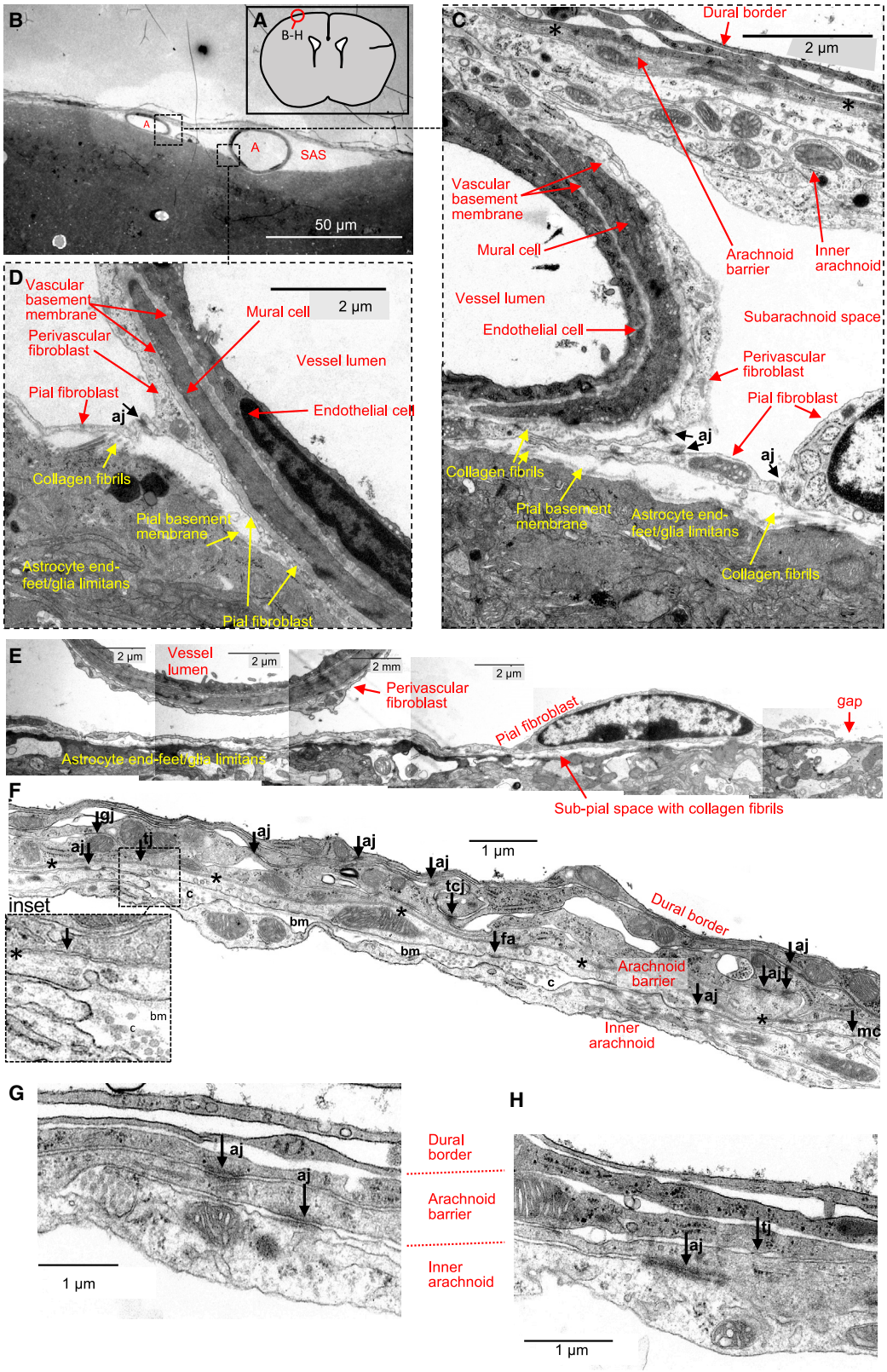

(legend on next page)

Please cite this article in press as: Pietilä et al., Molecular anatomy of adult mouse leptomeninges, Neuron (2023), https://doi.org/10.1016/j.neuron.2023.09.002

membrane (BM) production. BFB2 and BFB3 transcriptomes were both enriched in *Fmod* (fibromodulin), solute carrier *(Slc) 13a3*, and *Mapk4* (mitogen-activated protein kinase 4), but only BFB2 was enriched in *Sidt1* (SID1 transmembrane family member 1) and only BFB3 was enriched in *Ppp1r1a* (protein phosphatase 1 regulatory inhibitor subunit 1A) and *Slc22a8*. BFB4 transcriptomes were enriched in *Dpp4* (dipeptidyl peptidase IV), *Msln* (mesothelin), and *Cubn* (cubilin). BFB5 transcriptomes were enriched in *Slc47a1*, *Slc4a10*, *Slc23a2*, *Atp1b1* (ATPase Na+/K+ transportin subunit beta 1), and *Nov* (nephroblastoma overexpressed, a.k.a. *Ccn3*), among other molecular transporters. BFB6 was distinguished by enrichment of *Tcf21* (transcription factor 21), *Moxd1* (monooxygenase DBH like 1), *Emcn* (endomucin), *Dpep1* (dipeptidase 1), *Pgf* (placenta growth factor), *Lpl* (lipoprotein lipase), and other markers not found in BFB1–5.

Most dural FB transcriptomes had higher expression of several collagens and were distinct from BFB1–6, apart from similarities to BFB5 (Figures 1D and S2). Dural FB transcriptomes were heterogeneous, suggesting multiple distinct dural FB subtypes. These were not analyzed further because of the focus on FBs in the leptomeninges and brain.

When compared with FB transcriptomes from heart, skeletal muscle, large intestine, and bladder, similarly generated by SmartSeq2,[44] the BFB1–6 transcriptomes distributed close together in UMAP and were separated from FB transcriptomes from the other organs (Figure 1F). BFB1–6 transcriptomes included *Col1a1*, *Col1a2*, *Dcn*, and other canonical markers of FBs and lacked canonical markers of other cell types. Exceptions included low or absent expression of the common FB marker *Pdgfra* in BFB3, BFB4, and BFB5; presence of the epithelial marker *Cdh1* (E-cadherin) in BFB4 and BFB5; and the presence of the EC marker *Cdh5* (vascular endothelial [VE] cadherin) in BFB1, BFB2, BFB3, and BFB5.

BFB1–6 lacked significant expression of keratins, epithelial claudins, and other canonical epithelial markers, as well as endothelial markers *Pecam1*, claudin (*Cldn*)*5*, and *Kdr* (kinase insert domain receptor, a.k.a. vascular endothelial growth factor receptor 2) (see links to searchable databases in Figures S1–S4), underscoring their dissimilarity to epithelial cells or ECs. Choroid plexus epithelial cells and Epend cells were included as brain epithelial cell types for comparison (Figure 1F). BFB1–6 subtypes clustered apart from Epend cells but closer to (and yet still separate from) choroid plexus epithelial cells (Figure 1F′), which were also separate from dural border cells (BFB5) that clustered with dural FBs (Figure S2). Together, these data suggest that BFB transcriptomes derive from an organotypic sub-branch of the FB family. Among these, BFB1–5 appear most closely related to dural FBs, which reportedly have the same developmental origin.[3]

Matching BFB1–6 markers to previous scRNA-seq atlas data, without cell-type bias from brain regions in adult mice of similar age to our study,[43] revealed a close resemblance of BFB1–5 to previously described FL1–5[43] (Figure S5A), whereas BFB6 markers instead matched transcriptomes from adult choroid plexus FBs.[32] This concordance is evidence that BFB1–6 transcriptomes comprehensively cover the brain and leptomeningeal FB landscape.

To determine the developmental age at which BFB1–6 transcriptomes can be identified, we analyzed scRNA-seq data from 20- to 30-day-old (adolescent) mice[29] and embryonic mice at various stages of brain development.[14] Cells resembling BFB1–5 were found at adolescence (Figure S5B), but BFB6 cells typical of the choroid plexus (see below) were absent, presumably because the ventricles were excluded.[29] Embryonic BFB clusters resembled all six adult BFB subtypes without indications of additional major subtypes (Figure S6A). Cells with BFB1, BFB2, and BFB6 markers were already present at embryonic day (E) 11–12, whereas cells with BFB3, BFB4, and BFB5 markers were found from E13 to E13.5 (Figure S6B). Further comparison of BFB1–6 markers to published scRNA-seq data from E14.5 mouse meninges[48] confirmed the similarities between BFB1–5 and the four major groups of meningeal cells reported.[48] Thus, BFB1–6 cells emerge during midgestational embryonic development.

Ultrastructure of adult mouse leptomeninges

Analysis of cross-sections of the leptomeninges overlying the adult mouse brain by transmission electron microscopy (TEM) revealed multiple layers of FL with distinctive morphologies (Figures 2A–2H), confirming the pioneering observations made by the Reese and Brightman laboratories.[13] In our specimens, the SAS was collapsed over most of the brain surface but remained open around leptomeningeal arteries (Figure 2B) and at the longitudinal fissure (Figures S7B and S7C).

The BM of glia limitans astrocyte endfeet was covered by a single layer of thin (≈50–200 nm) pial cells interconnected by adherens junctions (Figures 2C and 2E), which had the ultrastructural features of adhesive junctions, as originally described.[49] The pial cell layer was continuous with cells of comparable ultrastructure surrounding mural cells of leptomeningeal blood vessels (Figures 2C–2E). Collagen fibrils were located between the glia limitans and the pia, and between perivascular FBs (PVFs) and vascular BMs (Figures 2C and 2D).

The SAS was bordered on the outside by the arachnoid membrane, which remained attached to the brain surface after the

Figure 2. Ultrastructure of adult mouse leptomeninges

(A) Schematic showing approximate location of specimens.

(B) Overview image of leptomeninges showing cross-sections of two leptomeningeal arteries (A) and the subarachnoid space (SAS), which is wide around arteries but narrow over most other regions of the brain surface.

(C and D) Higher-magnification views of the inset in (A) with relevant structures labeled.

(E) Montage of consecutive photos of a single pial cell over the glia limitans. Scattered gaps separate pial cells in some regions.

(F–H) Higher-magnification view of outer leptomeninges with main layers labeled.

aj, adherens junction; BM, basement membrane; gj, gap junction; fa, focal adhesions; tj, tight junction; PVF, perivascular fibroblast.

Scale bars and their lengths are provided individually for each panel (B–H). Asterisks in (F) indicate the close contact between ABCs.

Please cite this article in press as: Pietilä et al., Molecular anatomy of adult mouse leptomeninges, Neuron (2023), https://doi.org/10.1016/j.neuron.2023.09.002

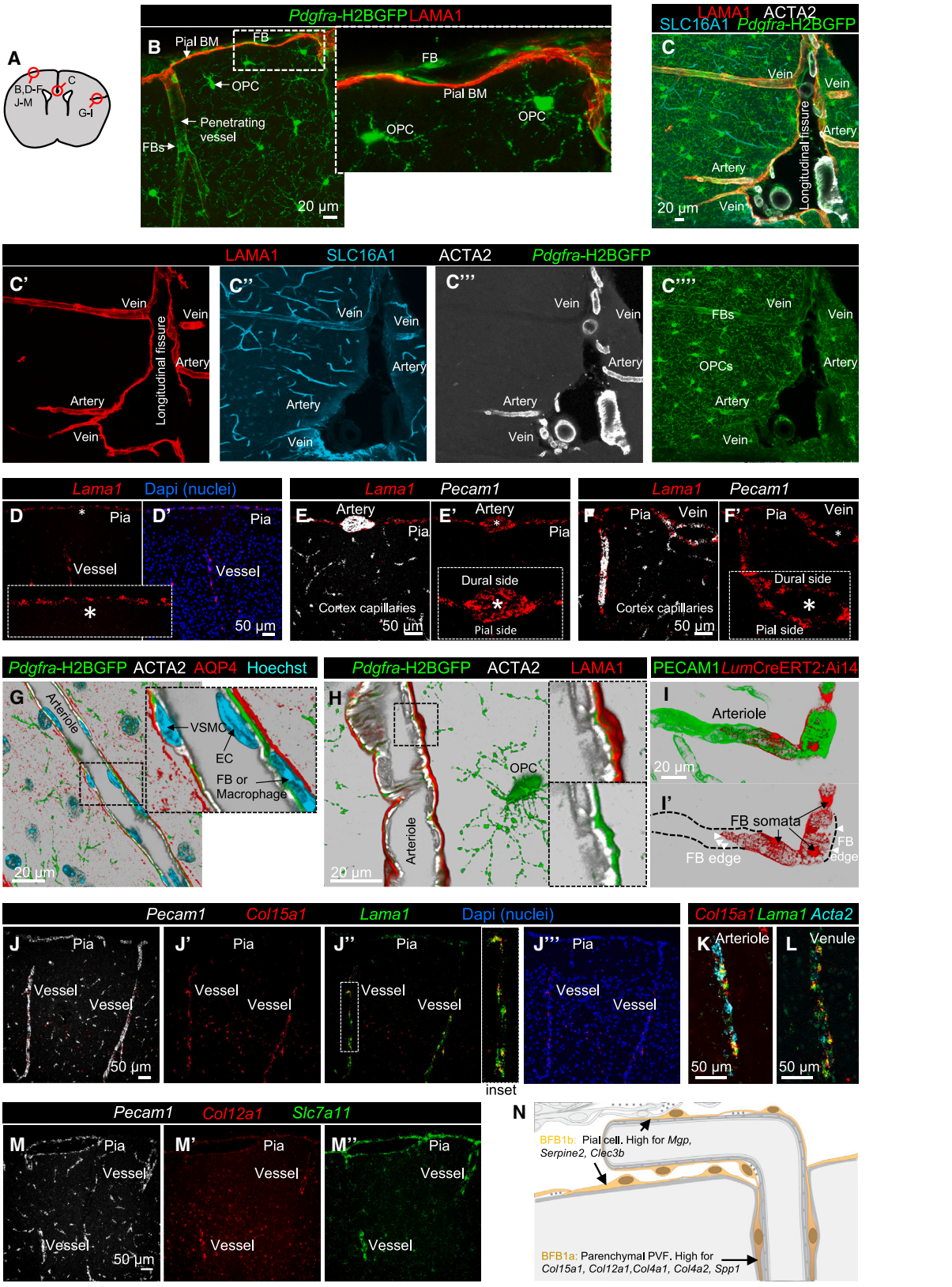

(legend on next page)

Please cite this article in press as: Pietilä et al., Molecular anatomy of adult mouse leptomeninges, Neuron (2023), https://doi.org/10.1016/j.neuron.2023.09.002

skull was removed. This membrane consisted of multiple layers of cells with distinct ultrastructure and electron density. One to several layers of electron-lucent cells (inner arachnoid layer) were above the SAS (Figures 2C and 2F). These cells were interconnected by adherens junctions, had a discontinuous BM, and were accompanied by scattered bundles of collagen fibrils (Figure 2F). The layer above the inner arachnoid consisted of a continuous sheet of cells, having the intermediate electron density and location described for ABCs.[13,50] Plasma membranes of adjacent cells in this layer were closer and their intercellular spaces more uniform in width than those of the inner arachnoid (asterisks in Figure 2F). Consistent with previous reports of tight junctions as a distinguishing feature of ABCs,[13,24,51,52] the plasma membrane of adjacent cells in this layer had points of seemingly fused outer leaflets, consistent with tight junctions (Figures 2F and 2H).[13] Adherens junctions were also abundant in this layer (Figures 2F–2H). A caveat of our observations is that TEM tracer studies or freeze fracture replicas would be needed for confirmation of tight junction identification.[13]

The outermost layer of the arachnoid consisted of morphologically distinct, thin electron-dense cells (Figures 2C and 2F–2H), similar to those described as dural border cells.[13,21] These cells were interconnected by adherens junctions but lacked interspersed collagen fibrils, unlike the inner arachnoid cells (Figure 2F) and dural FBs (Figure S7D).

Our TEM findings do not support the recent claim that the SAS is divided into inner and outer compartments.[53] Instead, our data confirm earlier evidence[13] that the inner arachnoid cells next to the SAS are connected to ABCs by adherens junctions with no intervening "outer SAS compartment." Instead, they argue that the outer SAS compartment is an artifactual subdural space. Overall, our TEM data, like those of others,[13] provide evidence that adherens junctions interconnect all layers of inner arachnoid cells, ABCs, and dural border cells. The broad distribution of adherens junctions is consistent with all arachnoid layers functioning as a single membrane composed of multiple interconnected cell types having different properties.

BFB1 identifies pial FBs and PVFs

We used immunofluorescence and RNAscope *in situ* hybridization (ISH) analysis with signature markers for each BFB type to establish their anatomical localizations. Immunoelectron microscopy (immuno-EM) and transgenic reporters were also used when possible. *Lama1* was one of the transcripts enriched in BFB1 (Figure 1E). We and others previously reported the presence of *Lama1*/*Pdgfra*-positive PVFs and LAMA1 in brain blood vessels[28] and glia limitans,[18] as confirmed in the present study (Figures 3A–3C). A continuous layer of LAMA1 also followed arteries (alpha-smooth muscle actin [ACTA2]-positive) and veins (SLC16A1-positive) penetrating the brain parenchyma but stopped at capillaries (Figures 3C′–3C‴) and did not surround pial blood vessels (Figures 3C and 3C‴). *Lama1* ISH decorated vessels in the pia and the brain (Figures 3D–3F), but surprisingly also marked LAMA1-negative pial vessels (Figure 3E′), consistent with the presence of perivascular *Lama1*-positive BFB1 cells that do not contribute LAMA1 protein to the vascular BM. To test this possibility, we used a *Pdgfra*-driven cytoplasmic GFP reporter (*Pdgfra*-GFP) to label BFB1 cells within the brain parenchyma in combination with aquaporin 4 (AQP4) staining of perivascular astrocyte endfeet and LAMA1 staining of vascular BMs (Figures 3G and 3H). A thin rim of *Pdgfra*-GFP-positive cytoplasm was visible between AQP4-positive astrocyte endfeet and ACTA2-positive vascular smooth muscle cells (VSMCs) (Figure 3G), confirming our previous observations of brain PVFs.[28] LAMA1 staining was observed on the astrocyte endfoot (outer) side of *Pdgfra*-GFP-positive cells but not on the (inner) side facing VSMCs (Figure 3H), suggesting that astrocyte endfoot contact is required for LAMA1 deposition by BFB1 cells. This finding is also consistent with the absence of BFB1-cell deposition of LAMA1 on pial vessels, which lack astrocytic endfoot coverage (Figures 3C and 3C‴).

The morphology of individual BFB1/pial cells was examined by TEM at sites where the SAS was visible near meningeal vessels (Figures 2C–2E). To further assess pial cell morphology, we generated a novel transgenic mouse (Tg*Lum*-CreERT2) in which tamoxifen-inducible CRE expression is controlled by the lumican (*Lum*) promoter (*Lum* was expressed in BFB1 and BFB2 and in BFB6 of choroid plexus FBs, see below). We then used genetic mosaic cell labeling by crossing Tg*Lum*-CreERT2 with Ai14 mice. Sparse Ai14 labeling revealed thin, large-diameter individual intracerebral BFB1 cells around arterioles (Figures 3I and 3I′).

We then asked whether pial FBs differ from FBs along perivascular spaces. *Lama1* mRNA and LAMA1 protein expression were evident along pial and parenchymal arterioles and venules, but ISH for the BFB1 markers *Col15a1* and *Col12a1* was strong along parenchymal arterioles and venules, but weak in the pia (Figures 3J–3M). To determine whether this correlated with other marker differences, we analyzed BFB1 transcriptomes across available datasets and found a skewed distribution of *Col15a1*- and *Col12a1*-high cells in the FL1 cluster from Saunders

Figure 3. Location and morphology of BFB1 cells

(A) Schematic showing approximate locations of the images.

(B and C) Confocal images of immunofluorescence and transgenic reporter expression. FB(s), fibroblast(s); BM, basement membrane; OPC, oligonucleotide progenitor; Mac, perivascular macrophage; EC, endothelial cell; VSMC, vascular smooth muscle cell.

(D–F) ISH for selected transcripts. Insets show enlargements of regions marked by an asterisk. N = 4 mice analyzed by *Lama1* ISH with similar results.

(G–I) Composite confocal images of immunofluorescence and transgenic reporter. In (I), the image shows the outline of individual perivascular BFB1 cells after mosaic labeling (6-month-old male). Images are representative of multiple sections from 3 tamoxifen-induced mice. No reporter expression was seen in one control mouse that did not receive tamoxifen. FB, fibroblast; Mac, perivascular macrophage; EC, endothelial cell; VSMC, vascular smooth muscle cell.

(J–M) ISH for selected transcripts. Insets are enlargements of region in hatched box. N = 3 mice analyzed for *Col15a1* and N = 2 mice for *Col12a1* ISH with similar results.

(N) Schematic showing BFB1a fibroblasts of the pia and covering pial vessels and BFB1b fibroblasts, with enriched candidate transcripts, along a vessel penetrating the CNS.

Scale bars and their lengths are provided individually for each panel (B–M).

Please cite this article in press as: Pietilä et al., Molecular anatomy of adult mouse leptomeninges, Neuron (2023), https://doi.org/10.1016/j.neuron.2023.09.002

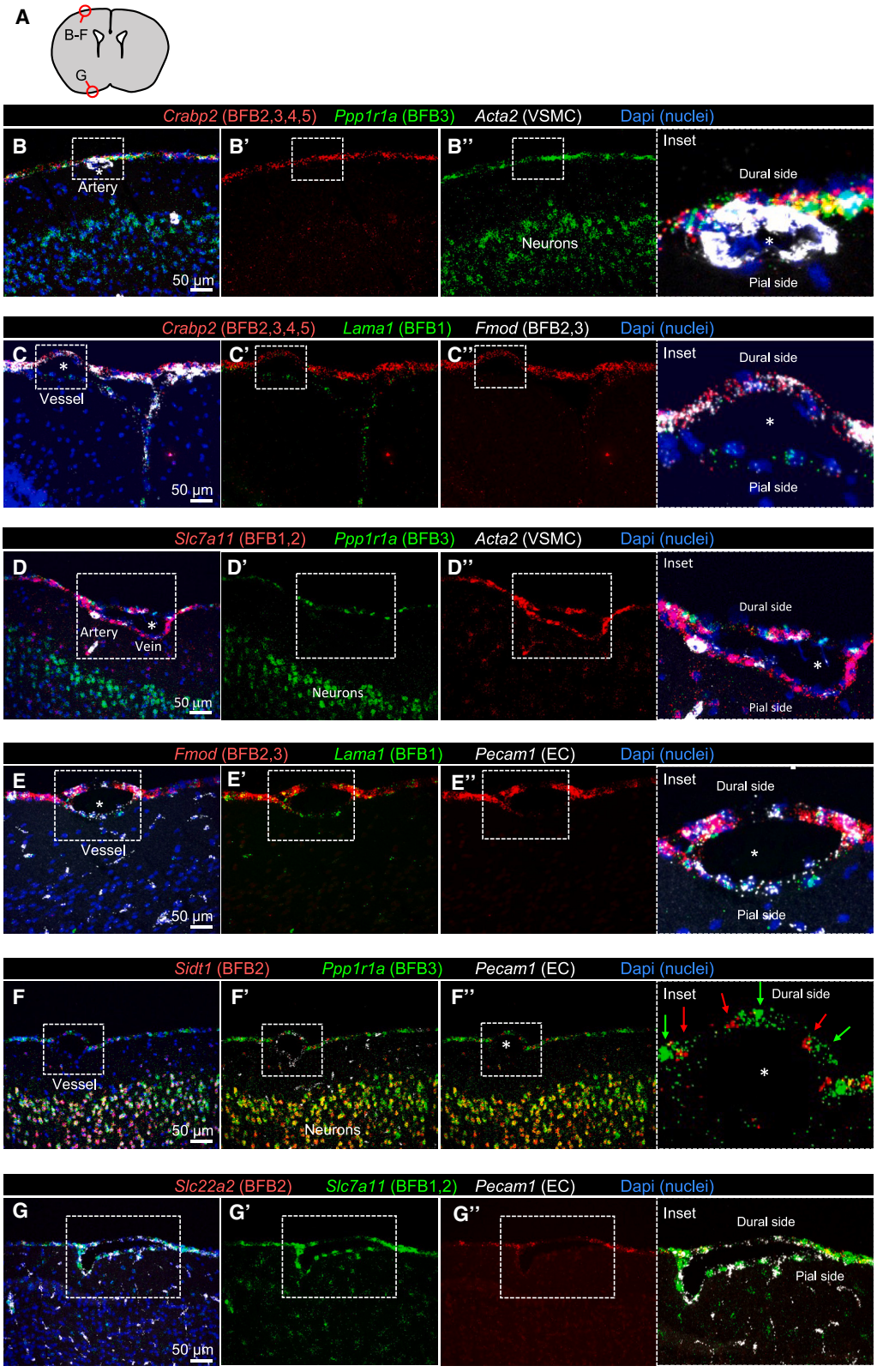

(legend on next page)

et al.[43] (Figures S7E–S7G). Several other markers co-segregated with *Col15a1* and *Col12a1*, including BM collagens *Col4a1* and *Col4a2*. A smaller number of mRNAs, including *Mgp* (matrix gla protein), *Pmepa1* (prostate transmembrane protein, androgen induced 1), *Serpine2* (serine protease inhibitor E2), and *Clec3b* (C-type lectin domain family 3, member b), showed lower expression at the perivascular location. This finding and the ISH distribution of *Col15a1* and *Col12a1* provide evidence that the BFB1a subtype transcriptome (*Col15a1*^{high}) marks parenchymal (but not pial) PVFs, whereas the BFB1b (*Col15a1*^{low}) transcriptome marks FBs of the pia and neighboring blood vessels (Figure 3N).

BFB2 and BFB3 identify two subtypes of inner arachnoid FBs

To determine the anatomical location of cells marked by the BFB2 and BFB3 transcriptomes, we first performed ISH for BFB2 and BFB3 signature markers (Figures 1E, S1, S4, and S5). *Crabp2* (cellular retinoic acid binding protein 2), enriched in BFB2–BFB5 but not in BFB1, uniformly labeled the brain surface but not the penetrating vessels (Figures 4A–4C), and was distributed on the outer (dural) side of pial blood vessels (Figures 4B and 4C). This finding is consistent with the association of *Crabp2* expression with arachnoid cells but not those of the pia.[48] *Ppp1r1a*, a marker of BFB3, also distributed on the outer side of pial vessels (Figures 4B, 4D, and 4F). In contrast, *Slc7a11*, enriched in BFB1, BFB2, and BFB6 (Figure S1B), distributed on both outer and inner (brain) sides of leptomeningeal vessels (Figures 4D and 4G), consistent with expression in both the pia (BFB1) and the arachnoid (BFB2). *Slc22a2*, a marker for BFB2, was not seen in *Slc7a11*-positive BFB1 cells at the inner side of the pial vessels (Figure 4G). *Fmod*, enriched in BFB2 and BFB3 (Figure S4B), distributed on the outer side of pial vessels (Figures 4C and 4E; the *Fmod* signal also present along penetrating vessels [Figure 4C] likely reflected expression in VSMC).[28] To determine the spatial relationship of BFB2 and BFB3, we performed co-ISH for *Sidt1* (a marker of BFB2 and neurons) and *Ppp1r1a* (BFB3). These signals did not overlap but were at a similar horizontal level, suggesting alternating positions of BFB2 and BFB3 in the arachnoid (Figure 4F). Collectively, these results place both BFB2 and BFB3 transcriptomes in the arachnoid.

Prox1 (prospero homeobox 1)-EGFP expression was recently reported to mark a previously unrecognized fourth layer of meninges.[53] We addressed this issue by using *Prox1*-EGFP reporter mice, which corroborated our finding of *Prox1* mRNA specifically in BFB3 and enabled further mapping of the distribution of BFB3 cells. *En face* views of vibratome sections cut from the dorsal cerebral surface revealed *Prox1*-EGFP-fluorescent cells immediately beneath a continuous layer of DPP4/CDH1 double-positive ABCs (Figures 5A–5C). These observations confirm the location of *Prox1*-EGFP cells and BFB3 transcriptomes in the inner arachnoid. ISH provided further confirmation that both BFB2 and BFB3 cells were located in the inner arachnoid (Figures 4B–4G).

BFB4 identifies ABCs, and BFB5 identifies dural border cells

E-cadherin (CDH1), a known marker of ABCs,[18,54] was expressed by BFB4 and BFB5 and found in the outer part of the arachnoid membrane (Figures 5B and 5C). Consistent with evidence that markers of BFB4 and BFB5 identified different cell populations, we found that double ISH for two BFB4 markers, *Dpp4* and *Slc7a14*, had overlapping expression in the arachnoid (Figure 5D), but *Dpp4*-labeled cells were distinct from cells labeled for the BFB5 marker *Slc47a1* (Figure 5E). Similarly, at the longitudinal fissure, double ISH/immunofluorescence labeling placed *Slc47a1*-positive cells outside the DPP4-positive cell layer (Figure 5F). Immuno-EM for DPP4 marked cells of intermediate electron density at the expected location of ABCs: above the inner arachnoid layer and beneath dural border cells (Figures 5G–5I). Together, these data connect the BFB4 transcriptome to ABCs and the BFB5 transcriptome to dural border cells.

scRNA-seq data showed that dural FB transcriptomes were similar to the BFB5 transcriptome (Figure S2D), although dural FBs and dural border cells were ultrastructurally distinct (compare Figures 2C and 2F–2H with Figure S7D). We found that gene ontology (GO) terms related to transmembrane molecular transport and cell junctions were significantly enriched in the BFB5 transcriptome, whereas terms related to collagen fibril organization, extracellular matrix, and vascular development were enriched in dural FB transcriptomes (Figure S2E; Tables S1 and S2). These results fit with the lack of collagen fibrils and blood vessels in spaces between dural border cells (Figures 2C and 2F–2H), whereas the dura was vascularized and had large bundles of intercellular collagen fibrils (Figure S7D).

Cellular and junctional organization of the AB

The AB contains intercellular tight junctions and is functionally defined by restricted mobility across the membrane of tracers placed on either side of the arachnoid.[55,56] CLDN11 has previously been found in the AB.[57] Using the scRNA-seq data, we confirmed the abundance of *Cldn11* and *Tjp1* (tight junction protein 1, a.k.a. zonula occludens 1 ZO-1) in BFB4 transcriptomes (Figure S8). In BFB4, we also found transcripts for the tricellular junction proteins angulin-1 (a.k.a. *Lsr* [lipolysis stimulated lipoprotein receptor]) and angulin-3 (a.k.a. *Ildr2* [immunoglobulin like domain containing receptor 2]), encoding tricellular proteins necessary for barrier integrity.[58] All of these tight junction transcripts were also found in BFB5 transcriptomes.

Figure 4. Relationship of BFB2 and BFB3 cells to vessels in leptomeninges

(A) Schematic showing approximate location of images.

(B–G) ISH for selected transcripts. The distribution of probe signals is shown relative to leptomeningeal blood vessel profiles marked by asterisks. Arterio-venous identity is indicated where conclusively shown by transcript/protein expression. Red/green arrows in (F) indicate non-overlapping pattern of the signal from different cells. N = 2 mice analyzed for *Crabp2*, N = 3 mice for *Ppp1r1a*, *Slc7a11*, and *Sidt1* expression and N = 4 mice for *Lama1* and *Fmod* expression. Scale bars and their lengths are provided individually for each panel (B–G).

Please cite this article in press as: Pietilä et al., Molecular anatomy of adult mouse leptomeninges, Neuron (2023), https://doi.org/10.1016/j.neuron.2023.09.002

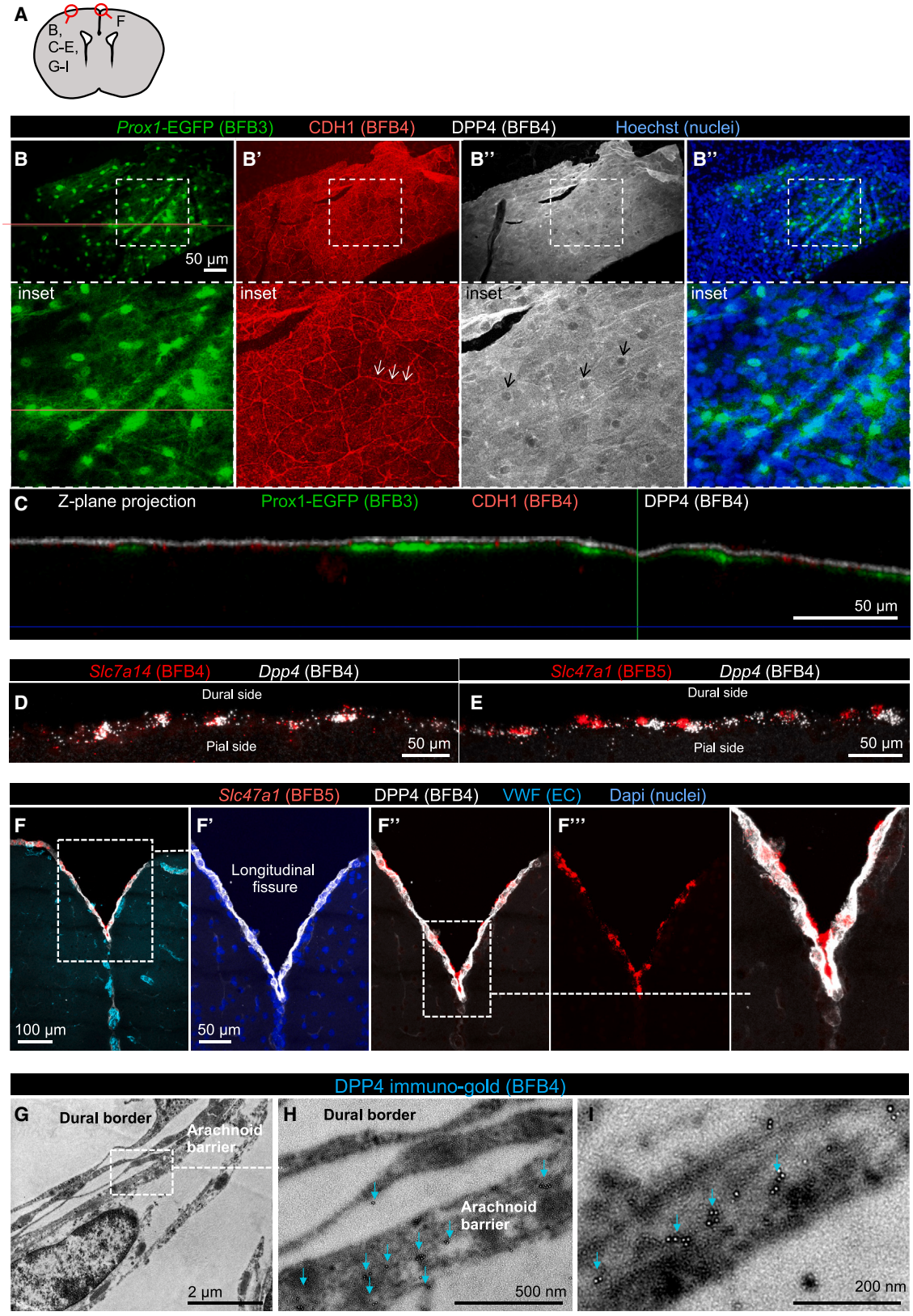

(legend on next page)

The distribution of junctional proteins revealed additional features of the junctions in the AB. Immunofluorescent triple labeling for CDH1, CLDN11, and LSR revealed all three proteins at cell borders in *en face* views of the arachnoid (Figure 6A). The distribution of CLDN11 suggested the presence of *zonula occludens* contacts at the lateral cell edges. CDH1 and CLDN11 also co-labeled dense focal contacts over the cell surface, consistent with focal adhesions to the extracellular matrix and/or vertically oriented *zonula adherens* and *zonula occludens* (Figure 6A) connecting two or more layers of ABCs.

Four additional observations further supported the existence of two layers of ABCs. First, the linear distribution of LSR, which differed from previous reports of LSR as spots at tricellular contacts in epithelial or brain EC monolayers,[59] is consistent with edge-to-edge tight junctions in one cell layer being "sealed" by tricellular junctions with overlapping cells in the second layer. Second, high magnification confocal Z scans identified neighboring ABC nuclei enwrapped by distinct DPP4-positive cell membranes at different z planes (Figure 6B). Third, ABC overlap was also shown by mosaic labeling of ABCs in *Cldn11*-CreER-T2:Ai14 mice (Figure 6C). The low degree of chimerism in these mice allowed visualization of the shape of individual ABCs, which were flat, uniform in area, 50–100 μm in diameter, and had one or two centrally positioned nuclei. Overlapping cells were revealed by junctional staining for CDH1, where multiple Ai14-positive cells were in direct contact (Figure 6C). Fourth, TEM images of vertical cross-sections of a continuous ≈50-μm-long stretch of arachnoid membrane provided evidence that ABCs form two overlapping layers connected by tight junctions, adherens junctions, and tricellular junctions (Figure 6D). These four lines of evidence are consistent with a two-layer arrangement of ABCs in which linear edge-to-edge contacts visible *en face* represent tricellular junctions between overlapping ABCs (schematically illustrated in Figure 6E).

Other features of the ABCs revealed by TEM included the presence of caveolae (Figure 6F) in both cell layers, which was consistent with the higher expression of caveolins (*Cav1, Cav2*) and clathrin heavy chain (*Cltc*) in BFB4 than in other BFBs (Figure 6G). Moreover, many collagen bundles were next to BMs attached to the inner layer of ABCs (Figure 6D).

BFB6 identifies a FB subtype near fenestrated blood vessels in the brain

To identify the cells corresponding to BFB6 transcriptomes, we took advantage of the BFB6 markers *Tcf21* and *Emcn* (Figure 1E). We generated *Tcf21-CreERT2* mice, crossed them with Ai14 mice, and found reporter expression specifically in the choroid plexus stroma (Figures 7A–7C). Stellate-shaped cells labeled by EMCN-immunofluorescence and by the FB marker *Pdgfra*-H2BGFP were scattered around choroid plexus capillaries (Figure 7D). BFB6-specific markers *Dpep1* and *Moxd1* (Figure S4B) co-localized with *Pdgfra* in the choroid plexus (Figures 7E–7G). In agreement with the scRNA-seq data, BFB6 cells also expressed some markers shared by other BFB transcriptomes (*Slc7a11* and *Col12a1*) and lacked expression of others (*Slc22a2* and *Slc47a1*) (Figures 7H–7J). *Slc47a1* was, however, found in a small population of *Dpep1*-negative cells in the hilar regions of the choroid plexus (Figure 7J″), but their nature and possible resemblance to dural cells require further study. *Dpep1* and *Tcf21*-CreER-T2:Ai14-positive BFB6 FBs were also found in the median eminence (Figures 7K and 7L), a neuroendocrine organ with fenestrated capillaries similar to those of the choroid plexus. Together, these findings provide evidence that BFB6 marks a subtype of BFBs distinctively associated with fenestrated capillaries in the choroid plexus and median eminence. Determining whether BFB6 FBs contribute to the presence of fenestrations in neighboring ECs or to the barrier function of overlying epithelial cells awaits further studies.

BFB markers in leptomeninges of the spinal cord

The characterization of the BFB1–6 transcriptomes as FB markers provides tools to compare the leptomeninges in the brain and spinal cord. The extent of molecular and cellular similarity of the leptomeninges in the brain and spinal cord is unclear, and the scarcity of FB data in public datasets for spinal cord scRNA-seq[60,61] has limited analysis. To address this issue, we examined BFB markers in spinal cords in demineralized vertebral columns by immunofluorescent staining of selected markers for BFB transcriptomes. In the spinal cord, the pia and large (non-capillary) parenchymal vessels had LAMA1 labeling (Figures 8A–8C), and continuous layers of arachnoid cells had labeling for arachnoid cell markers CRABP2, CDH1, DPP4, and CLDN11 (Figures 8B–8E). In the spinal cord, the arachnoid was separated from the pia by a distinct SAS, which at the thoracic level also contained spinal nerve roots surrounded by a layer of DPP4-positive cells (Figure 8D) that may correspond to epineurial or perineural cells, which are *Dpp4*-positive and -negative, respectively.[62] We also found *Prox1*-EGFP-positive cells in spinal cord arachnoid (Figure 8E). As in the brain, these cells were located immediately beneath the CDH1-positive ABC layer (Figure 8E‴). The concordance of the distribution of markers for BFB1 (LAMA1) in the pia, BFB3 (*Prox1*-EGFP) in the inner

Figure 5. Location of Prox1-GFP (BFB3), BFB4, and BFB5 cells in leptomeninges

(A) Schematic showing approximate location of images.

(B) *En face* view of leptomeninges on dorsal cerebral surface of Prox1-GFP reporter mouse after co-staining for DPP4, CDH1 (E-cadherin), and Hoechst 33342 (nuclei). Line in (B) and inset indicates the level for z axis projection shown in (C).

(C) z axis projection of (B).

(D and E) ISH for *Slc7a14*, *Dpp4*, and *Slc47a1*. mRNA signals are concentrated over cell somata, where they have overlapping red/white distributions in (D) and non-overlapping distributions in (E). N = 2 mice analyzed.

(F) ISH/immunofluorescence combinations as indicated at the dorsal part of the longitudinal fissure.

(G–I) Immuno-EM against DPP4. Signal (gold grains marked by cyan arrows) is enriched over the cell layer of intermediate electron density located in the outer part of the arachnoid immediately beneath dural border cells. In (H) and (I), signals appear as round uniform refractile particles above the slightly out of focus tissue section.

Scale bars and their lengths are provided individually for each panel (B–I).

Please cite this article in press as: Pietilä et al., Molecular anatomy of adult mouse leptomeninges, Neuron (2023), https://doi.org/10.1016/j.neuron.2023.09.002

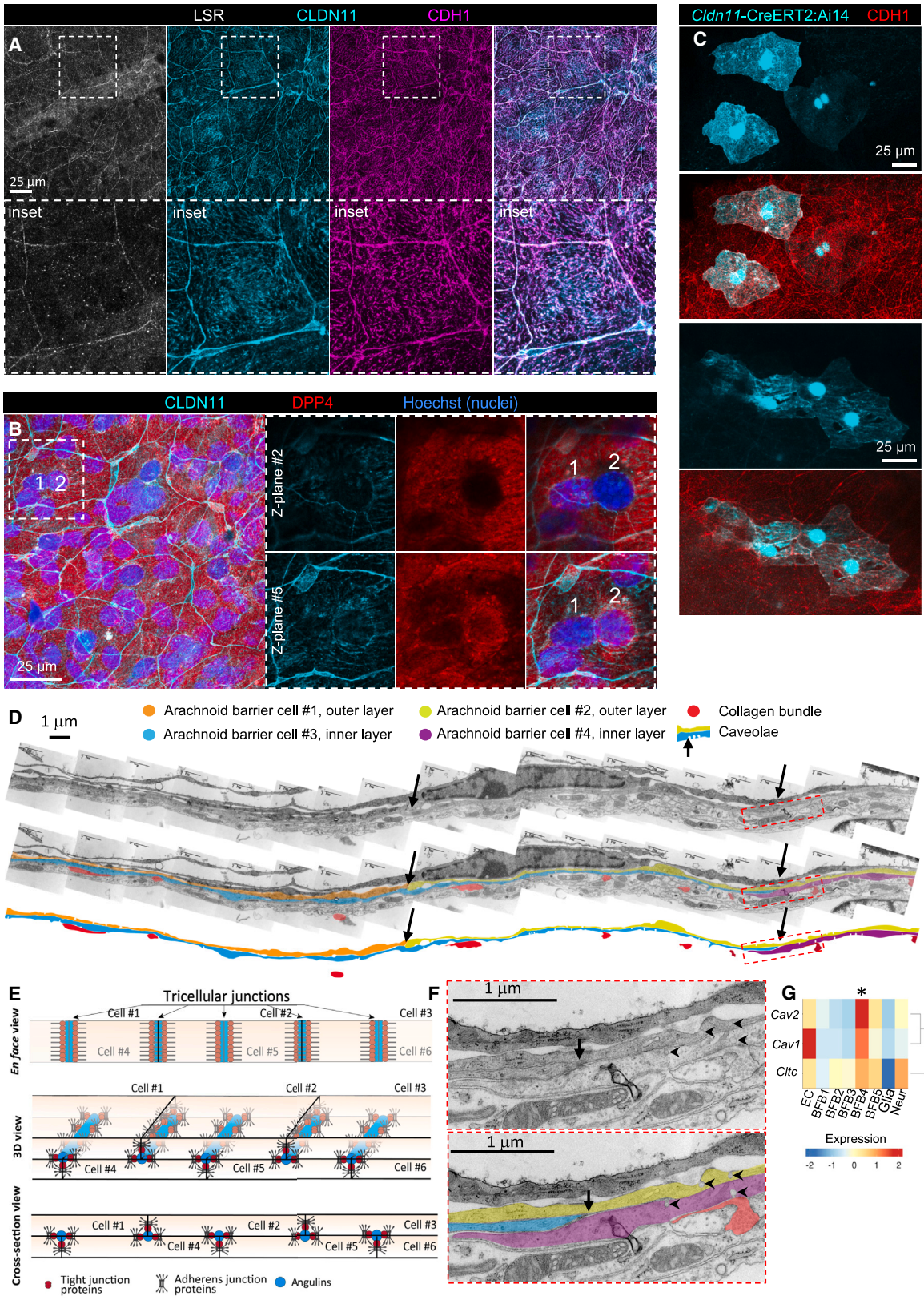

(legend on next page)

Please cite this article in press as: Pietilä et al., Molecular anatomy of adult mouse leptomeninges, Neuron (2023), https://doi.org/10.1016/j.neuron.2023.09.002

arachnoid, and BFB4 (DPP4 and CRABP2, CDH1 and CLDN11) in the AB is evidence of cellular and molecular similarities of brain and spinal cord leptomeninges.

Utility of BFB markers for elucidating responses to TBI

Previous scRNA-seq analysis of meningeal responses to TBI revealed extensive changes in FBs and influx of inflammatory cells into the dura, but single-cell transcriptomes from leptomeningeal cells were few or absent.[39] We therefore asked whether the markers of BFB1–5 transcriptomes would help to elucidate changes in leptomeningeal cell types after trauma or during repair. To address this question, we analyzed meninges after controlled cortical impact (CCI), a common model of focal TBI, induced by CCI to 2-mm depth by a 3-mm-diameter cylindrical piston at the center of an 8 × 8 mm cranial window of exposed dura.[63–67] At 28 days after TBI, we found that regrown dura and bone covered the wounded region. Careful removal of the dura exposed a thin translucent membrane over the cortical lesion cavity created by resorption of the damaged cortical tissue. Analysis of the injured region by ISH for BFB markers revealed *Fmod* (BFB2 and BFB3), *Dpp4* (BFB4), and *Slc47a1* (BFB5) expression in separate or overlapping cells within the translucent membrane covering the pit, indicating the presence of pial and arachnoid FBs (Figures 8G and 8H). Normal layering of markers identified by ISH after TBI appeared to be preserved. TEM analysis revealed cells with electron densities, junctions, and collagen bundles typical of the arachnoid, but the overall ultrastructure had multiple abnormalities (Figure 8I). These observations demonstrate the potential value of using BFB1–6 markers in future studies of meningeal pathology and recovery and to gain insights into arachnoid resilience versus repair.

DISCUSSION

Among the diverse cell types in the brain, FBs are now receiving greater attention because of their contributions to fibrotic reactions in trauma and inflammation.[33,34,68–70] FB heterogeneity and subtype-specific distributions in leptomeninges have previously been studied during development[48,54] and in perivascular spaces[28,36,71] and the choroid plexus[32] in the adult. To build on this background, we sought to map the BFB landscape broadly by applying a multipronged approach for cell isolation and scRNA-seq analysis. This approach turned out to be essential, because each method captured a different combination of FB transcriptomes. Another attribute was that transcriptomes from specific structures (leptomeninges, dura, or vascular fragments) naturally mapped to those structures when localized by transcriptome-specific markers.

A further attribute of the experimental design was the use of ISH, immunofluorescence, immuno-EM, and transgenic reporters to match BFB transcriptomes to anatomical structures and locations. This linked the BFB1a and BFB1b transcriptome to pial FBs and PVFs, respectively. Pial FBs had minor but distinct transcriptomic differences from PVFs, as exemplified by higher expression of *Col15a1* and certain other collagens in the latter. A subset of pial cells—referred to as epipia—have been reported to surround arteries near the ventral brain surface, based on morphology and detection by ERTR7 antibodies.[72] Consistent with ERTR7 antibodies binding collagen type 6,[73] we confirmed that both *Col6a1* and *Col6a2* are expressed by pial BFB1 transcriptomes. BFB2–5 transcriptomes marked four cell subtypes in the arachnoid, BFB2 and BFB3 in the inner arachnoid, BFB4 in ABCs, and BFB5 in dural border cells. TEM showed that the inner arachnoid layer was one to four cells in thickness, had a discontinuous BM, and was interspersed by collagen bundles, as expected for mechanical strength and resilience.

BFB3 inner arachnoid cells expressed *Prox1* and *Cdh5* and were interconnected by abundant adherens junctions. *Prox1* expression has been claimed to identify a previously unrecognized fourth meningeal membrane called the subarachnoid lymphatic-like membrane (SLYM).[53] The SLYM was reportedly located between the pia and the arachnoid, divided the SAS into two non-communicating compartments, and formed a barrier between these inner and outer compartments.[53] The SLYM, identified by fluorescence microscopy in reporter mice that express *Prox1*-EGFP, was considered molecularly unique.[53] Contrary to these claims, we found no evidence for a fourth meningeal layer between the pia and the arachnoid, or for inner and outer subdivisions of the SAS. Instead, we found a single SAS bordered by pial cells on the brain side and by the arachnoid on the skull side, as described in many previous

Figure 6. Cellular and junctional organization of the arachnoid barrier

(A) *En face* view of dorsal cerebral surface stained with antibodies against LSR, CDH1, and CLDN11. Insets show enlargements of indicated regions. LSR, CLDN11, and CDH1 signals overlap at lateral cell borders. CLDN11 and CDH1 signals also partially overlap over the horizontal cell surface(s). N = 3 mice analyzed with similar results.

(B) High magnification *en face* staining. Insets show two different optical z planes. CLDN11 and DPP4 co-staining of two partially overlapping arachnoid barrier cells (adjacent nuclei 1 and 2) enclosed by separate DPP4 positive cell membranes.

(C) Top panel: *en face* view of mosaic *Cldn11* reporter (cyan) labeling in non-overlapping arachnoid barrier cells illustrates their morphology and occasional binucleated feature. Middle and lower panels show partially overlapping *Cldn11* reporter and CDH1 positive cells consistent with a double layer of arachnoid barrier cells.

(D) TEM images showing a double layer of arachnoid barrier cells. Arrows in (C) and (D) mark region of tricellular contacts between arachnoid barrier cells.

(E) Schematic showing cellular and junctional arrangements in the arachnoid barrier.

(F) Enlargements of areas bordered by red hatched line in (C). The arachnoid barrier cells are artificially colored to show close apposition and location of tricellular contact (arrow). Arrowheads mark caveolae in both layers of arachnoid barrier cells. Collagen bundles near the inner arachnoid barrier cells are artificially marked by red color.

(G) Heatmap of caveolin-1 (*Cav1*) and-2 (*Cav2*) and clathrin heavy chain (*Cltc*) mRNA expression in selected cell types (data from Saunders et al.[43] displayed using ShinyCell).

Scale bars and their lengths are provided individually for each panel (A–D and F).

Please cite this article in press as: Pietilä et al., Molecular anatomy of adult mouse leptomeninges, Neuron (2023), https://doi.org/10.1016/j.neuron.2023.09.002

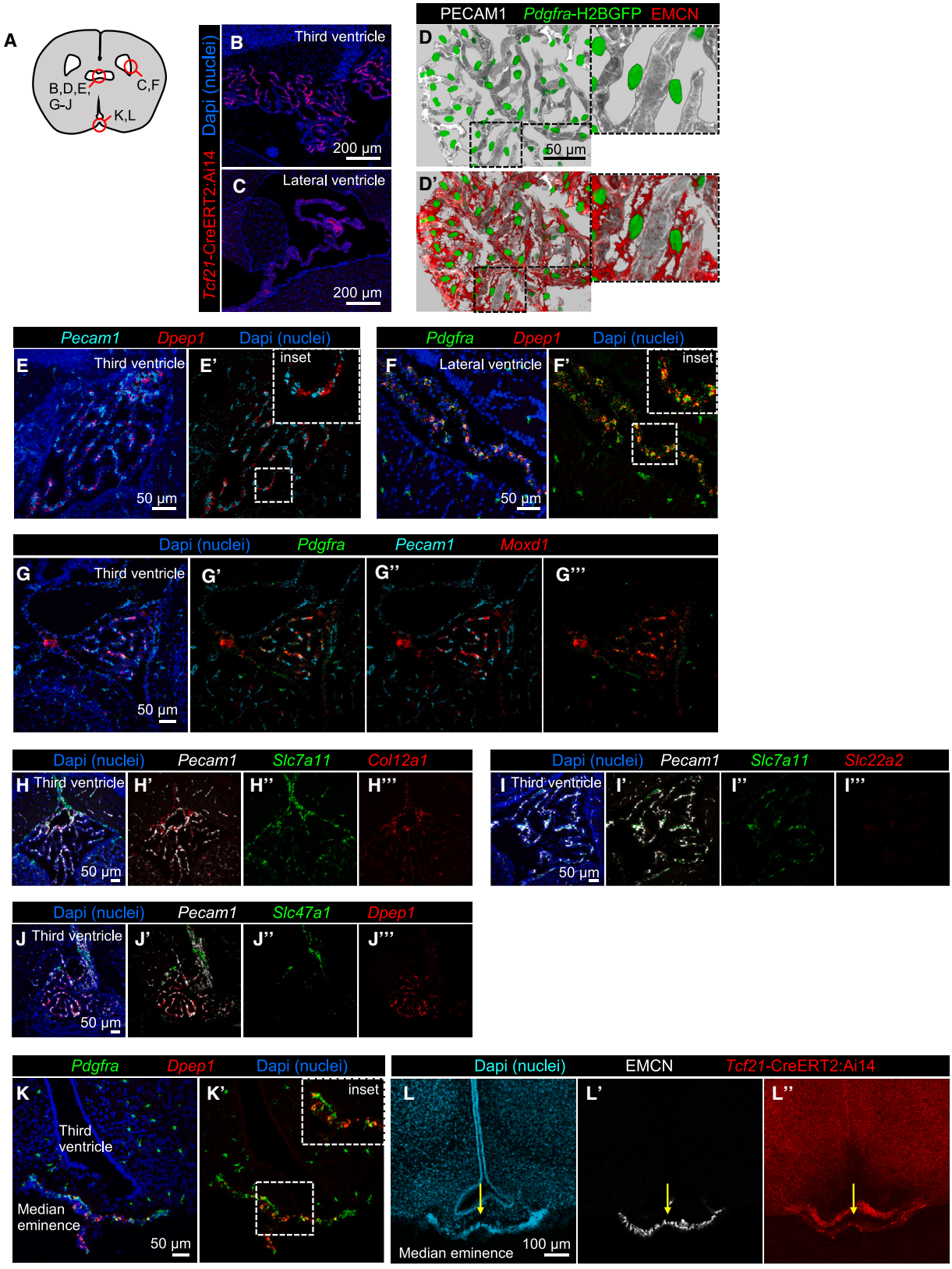

(legend on next page)

Please cite this article in press as: Pietilä et al., Molecular anatomy of adult mouse leptomeninges, Neuron (2023), https://doi.org/10.1016/j.neuron.2023.09.002

reports.[13,22,74–78] Although we found *Prox1* mRNA in BFB3 transcriptomes and *Prox1*-EGFP-positive cells in the inner arachnoid, our TEM analyses confirmed earlier observations[13] that inner arachnoid cells are connected to each other and to ABCs by adherens junctions and gap junctions. The presence of these junctions was further supported by expression of VE-cadherin (*Cdh5*) and connexins 43, 26, and 30 (encoded by *Gja1*, *Gjb2*, and *Gjb6*, respectively) in BFB2, BFB3, and BFB4 transcriptomes from these layers of the arachnoid.

The transcriptional annotations of the inner arachnoid, AB, and dural border cells shed new light on the molecular organization of barriers. ABCs are known to form a permeability barrier between the SAS and dura.[55,56] Informed by the BFB4 transcriptome, we unraveled overlapping layers of ABCs sealed by conventional bicellular tight junctions composed of CLDN11 and adherens junctions composed of CDH1 complemented by unusual tricellular junctions containing angulin-1 (LSR) and CLDN11. Additional components of tight, adherens, and tricellular junctions in ABCs were implicated through the presence of transcripts encoding ZO-1 (*Tjp1*), VE-cadherin (*Cdh5*), and angulin-3 (*Ildr1*) in the BFB4 transcriptome (Figure S8). DPP4, another BFB4 marker of ABCs, could add to the structural junctions by serving as an enzymatic barrier. TEM analysis confirmed that ABCs are tightly adherent to each other. By comparison, most cells of the dural border cell membrane appeared physically detached from one another and from adjacent cells, although scattered focal contacts of dural border cells had the ultrastructural features of adherens junctions, and BFB5 cells expressed multiple cadherin transcripts, including *Cdh1*, *Cdh5*, and *Cdh11* (Figure S8). Transcripts for classical desmosomal proteins were not found in any of the BFB transcriptomes, arguing against the notion that desmosomes constitute the contacts in the TEM images. Instead, all cell types within the arachnoid were interconnected by adherens junctions.

Several published scRNA-seq studies describe single-cell transcriptomes of BFBs, some of which are assigned to the leptomeninges based on reported markers for the pia, arachnoid, and dura.[48,79] These transcriptomes have been named *vascular leptomeningeal cells* (*VLMC*)*-1*, *VLMC-2*, and *ABCs*,[29] *FL1–5*,[43] and *Pia*, *FB arachnoid*, *AB*, and *Dura1–3*.[30] When comparing our data and cell-type annotations to these names, we conclude that *VLMC-1* corresponds largely to BFB1, *VLMC-2* to BFB2, *ABC* to BFB4 and BFB5,[29] and *FL1–5* to BFB1–5, respectively.[43] Pia corresponds to BFB1 and BFB2, FB arachnoid to BFB3, AB to BFB4 and BFB5, and *Dura3* to BFB5.[30] The concordance between our data and those of the previous studies argues that the BFB1–5 transcriptomes comprehensively cover the leptomeningeal FB subtypes and that the corresponding cell types identified in the pia and the arachnoid (summarized in Figure 1A) create a molecularly based anatomical map of the leptomeninges.

The transcriptomes and locations of BFBs at interfaces of the brain, SAS, meninges, and surrounding structures raise further questions about putative barrier functions of BFB1–6. In addition to the junctional molecules that create physical barriers, membrane-bound transporters and enzymes could contribute to transport and metabolic barriers. Examples include the differential expression of *Slc* and ATP-binding cassette (*Abc*) families of transporters among BFB subtypes (Figure S8). Differences in amino acid and sugar transport are accompanied by differential expression of neurotransmitter transporters; members of the *Slc1a* and *Slc6a* families of glutamate, GABA, and glycine transporters are selectively expressed by pial and inner arachnoid FBs. Moreover, the *Abca8/Abca9* family of lipid transporters is selectively expressed by pial and choroid plexus/median eminence FBs. The drug and xenobiotics transporters *Abcb1a* (a.k.a. P-glycoprotein [PGP]) and *Abcg2* (a.k.a. breast cancer resistance protein [BCRP]) were found in ABCs and dural border cells, confirming reported expression at the AB.[52] The drug transporters *Slc47a1*, *Slc47a2*, and *Abcc4* were selectively found in dural border cells and dural FBs. Similarly, drug-metabolizing enzymes were among the most strongly differentially expressed genes, examples being *Cyp1b1* (cytochrome P450 1B1) in pial, inner arachnoid, and choroid plexus FBs, *Dpp4* in ABCs, and *Ugt* (UDP glucuronosyltransferase) in choroid plexus FBs (Figure S8).

In conclusion, this work created a single-cell transcriptomic resource of BFBs, with a particular emphasis on a molecular anatomical map of FBs of the pia and the arachnoid. We demonstrate the utility of transcriptional markers of FB subsets in analyzing leptomeningeal cell types in the brain and spinal cord—normally, after injury, and during repair. These data also provide candidates for genetic targeting strategies and future research into the functional roles of BFBs under normal conditions and in neurodegenerative and neurovascular diseases, trauma, infection, and stroke.

Limitations of the study

Our analyses focused on the leptomeninges overlying the dorsal cerebral cortex and did not examine regional differences in molecular and cellular composition of the leptomeninges in other regions of the brain. Our analysis of the spinal cord confirmed expression of markers for the pia (LAMA1) and the arachnoid (CRABP2, CDH1, DPP4, CLDN11, and Prox1-GFP), and although the analysis demonstrated the utility of the markers and antibodies to identify them by immunofluorescence, we did not attempt to prove the cellular identity of cells in spinal

Figure 7. Location of BFB6 in the choroid plexus and median eminence

(A) Schematic showing approximate location of images.

(B–L) Fluorescent images of reporter (B, C, and L″), antibody (D and L′), or ISH (+Dapi) (E–J) labeling of sections of third or lateral ventricles, as indicated. Choroid plexus is central in each image and has a network of Pecam1-positive vessels with surrounding stromal fibroblasts labeled by indicated markers (epithelial cells are not visualized). Images labeled with the same letter and different numbers of apostrophes show different probes or combinations on same section. In (D), the images have gray background to show spatial relationships. (K and L) Shows coronal sections of median eminence labeled by indicated ISH probes (K), antibody (L′), or *Tcf21* reporter (L″). TCF21 reporter (red) labels two structures in median eminence, the lower of which overlaps EMCN (L′) near fenestrated capillaries (green arrows). N = 4 + 4 *Tcf21*-reporter mice analyzed. N = 2 mice analyzed for *Dpep1* mRNA expression in the choroid plexus and N = 1 mouse in median eminence. N = 2 mice analyzed for *Moxd1*, *Slc7a11*, *Slc47a1*, *Col12a1*, and *Slc22a2* expression.

Scale bars and their lengths are provided individually for each panel (B–L).

Please cite this article in press as: Pietilä et al., Molecular anatomy of adult mouse leptomeninges, Neuron (2023), https://doi.org/10.1016/j.neuron.2023.09.002

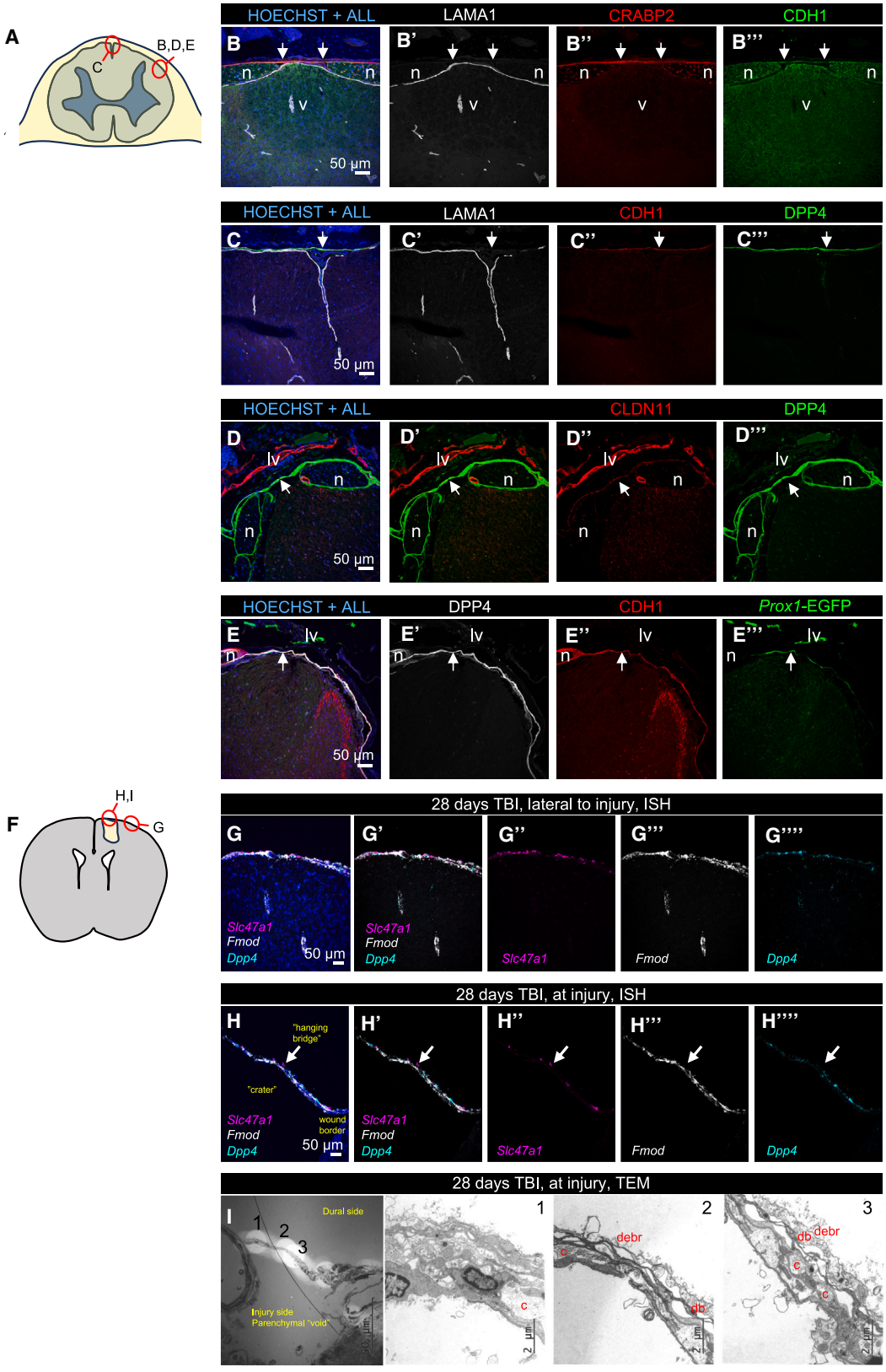

(legend on next page)

cord leptomeninges to corresponding cells in cerebral leptomeninges. For such proof, additional markers and scRNA-seq data for leptomeninges in different regions of the CNS would be needed. The same limitation applies to the similarity between FBs in the choroid plexus and median eminence. The larger size of the choroid plexus compared with the median eminence makes it likely that most, perhaps all, BFB6 transcriptomes obtained in our study were from the choroid plexus. For this reason, we could not distinguish choroid plexus FB transcriptomes from those in the median eminence.

STAR★METHODS

Detailed methods are provided in the online version of this paper and include the following:

- KEY RESOURCES TABLE
- RESOURCE AVAILABILITY
  - Lead contact
  - Materials availability
  - Data and code availability
- EXPERIMENTAL MODEL AND SUBJECT DETAILS
  - Animals
- METHOD DETAILS
  - Isolation of cells and scRNAseq
  - Single-cell RNA sequencing data analysis
  - Immunostaining of tissue sections
  - *In situ* hybridization (ISH)
  - Transmission electron microscopy (TEM)
  - Immuno-EM
  - Traumatic brain injury (TBI)
- QUANTIFICATION AND STATISTICAL ANALYSIS

SUPPLEMENTAL INFORMATION

Supplemental information can be found online at https://doi.org/10.1016/j.neuron.2023.09.002.

ACKNOWLEDGMENTS

We thank Cecilia Olsson, Pia Peterson, Jana Chmielniakova, Helene Leksell, Karin Staxäng, Monika Hodik, and the BioVis core for technical assistance at Uppsala University; Sonja Gustafsson, Byambajav Buyandelger, Elisabeth Raschperger, and the single-cell core at Campus Flemingsberg (SICOF) for technical assistance at Karolinska Institutet; and Karri Niiranen, Tanja Laakkonen, Tapio Tainola, the Flow Cytometry Unit at the Helsinki Institute of Life Sciences (HiLIFE), and the Laboratory Animal Center at HiLIFE for technical assistance at the University of Helsinki. We thank Drs. Mikio Furuse, Lydia Sorokin, and Philippe Soriano for kindly providing LSR antibodies, LAMA1 antibodies, and *Pdgfra*-H2BGFP mice, respectively. Financial support is acknowledged as follows: Swedish Research Council (C.B., 2015-00550; U.L., 2019:00285; T.M., 2020-02692); Swedish Cancer Society (C.B., 2018/449, 2018/1154, and 211714Pj); Knut and Alice Wallenberg Foundation (C.B., 2020.0057; T.M., 2018.0218); Swedish Brain Foundation (C.B. and U.L., ALZ2019-0130 and ALZ2022-0005; U.L., F2020-0246); Erling-Persson Family Foundation (H.K., U.L., P.N., E.P.T., and C.B.); Stiftelsen för åldersjukdomar vid KI (F.D.G., 2022:01310); Magn. Bergvalls Foundation (L.M., 2020-03735, 2021-04275, and 2022-158); Wenner-Gren foundations Fellows program (E.M.H.); Strategic Research Area Neuroscience (StratNeuro) (E.P.T.); Karolinska Institutet Funds (E.P.T., 2022-01576); Region Stockholm ALF (E.P.T., FoUI-962566); Region Stockholm Clinical Research Appointment (E.P.T., FoUI-981490); Karolinska Institutet Clinical Scientist Training Program (C.L.); Karolinska Institutet Research Internship (C.L.); Uppsala University Hospital Research Residency Program (C.L.); Strategic Research Area Stem Cells and Regeneration (StratRegen) (M.V.); KI Infrastructure Council (M.V.); The European Research Council (ERC) under the European Union's Horizon 2020 research and innovation programme under grant agreement No 743155 (BrainDrain) (K.A.); Research Council of Finland Terva Program (grant 335721) and the Finnish Brain Foundation (K.A.); Swiss National Science Foundation Grant 310030_189080 (B.E.) and CRSII5_213535 (S.P. and B.E); Research Council of Norway (RCN) Grant 214458 (L.H.B. and J.S.-M.); National Heart Lung and Blood Institute of the US National Institutes of Health (D.M., R01HL143896, R01HL059157, and R01HL127402). Computations/data handling were enabled by the National Academic Infrastructure for Supercomputing in Sweden (NAISS) and the Swedish National Infrastructure for Computing (SNIC) at NAISS AFFILIATED SITE/SNIC CENTRE, partially funded by Swedish Research Council through grant agreements 2022-06725 and 2018-05973.

AUTHOR CONTRIBUTIONS

C.B., J.A., and U.L. conceived and designed the project. R.P. performed ISH, immunofluorescence, and reporter mouse analyses. F.D.G. performed reporter and TBI experiments and isolated cells for scRNA-seq analysis. L.H. performed bioinformatic analyses and constructed online databases. E.V.-L. performed immunofluorescence analyses. M.V., L.M., G.M., and J.L. performed scRNA-seq analyses. K.D.B., C.L., A.F.-S., M.S., and E.P.T. performed TBI experiments. A.J.v.V., M.T., and J.A. performed reporter and immunofluorescence analyses. S.A. performed scRNA-seq analysis of the dura mater. L.X. performed analysis of reporter mice. H.K. supervised K.D.B. J.S.-M. and L.H.B. contributed *Hcar1* reporter mice at an early stage of the project. A.M. and E.M.H. generated *Tcf21*-CreERT2 mice. M.H.U. contributed *Prox1*-GFP mice. M.V., P.N., and H.K. supported scRNA-seq analysis of brain vascular fragments. T.M. contributed Cldn11-CreERT2:Ai14 mice. M.A.M. supervised E.V.-L., K.A. supervised S.A., and S.T.P. supervised L.X. C.B., R.P., L.H., F.D.G., E.V.-L., M.A.M., K.A., S.T.P., B.E., D.M.M., U.L., and J.A. interpreted the data. C.B., L.H., R.P., E.V.-L., and M.A.M. designed illustrations. C.B., U.L., and D.M.M. wrote the manuscript. All authors reviewed and edited the text.

DECLARATION OF INTERESTS

The authors declare no competing interests.

Received: October 4, 2022
Revised: July 7, 2023
Accepted: September 5, 2023
Published: September 29, 2023

Figure 8. BFB marker expression in spinal cord leptomeninges and after traumatic brain injury (TBI)

(A) Schematic showing approximate location of spinal cord images.

(B–E) Immunofluorescence images of selected pial and arachnoid BFB markers. Arrows mark the arachnoid. v, vessel; n, nerve; lv, lymphatic vessel. (D) DPP4 also labels perineurial fibroblasts.

(F) Schematic showing approximate location of TBI.

(G and H) ISH of selected BFB markers at and around injury site. Arrows mark the leptomeninges over the pit created by resorption of damaged cortical tissue. N = 3 mice analyzed.

(I) TEM images of injured brain showing disorganized, regrown arachnoid membrane over injured region. Debr, debris; db, dural border cell; c, collagen. Scale bars and their lengths are provided individually for each panel (B–E and G–I).

REFERENCES

1. Kierdorf, K., Masuda, T., Jordão, M.J.C., and Prinz, M. (2019). Macrophages at CNS interfaces: ontogeny and function in health and disease. Nat. Rev. Neurosci. *20*, 547–562. https://doi.org/10.1038/s41583-019-0201-x.
2. Tietz, S., and Engelhardt, B. (2015). Brain barriers: crosstalk between complex tight junctions and adherens junctions. J. Cell Biol. *209*, 493–506. https://doi.org/10.1083/jcb.201412147.
3. Dorrier, C.E., Jones, H.E., Pintarić, L., Siegenthaler, J.A., and Daneman, R. (2022). Emerging roles for CNS fibroblasts in health, injury and disease. Nat. Rev. Neurosci. *23*, 23–34. https://doi.org/10.1038/s41583-021-00525-w.
4. Coles, J.A., Myburgh, E., Brewer, J.M., and McMenamin, P.G. (2017). Where are we? The anatomy of the murine cortical meninges revisited for intravital imaging, immunology, and clearance of waste from the brain. Prog. Neurobiol. *156*, 107–148. https://doi.org/10.1016/j.pneurobio.2017.05.002.
5. Tumani, H., Huss, A., and Bachhuber, F. (2017). The cerebrospinal fluid and barriers - anatomic and physiologic considerations. Handb. Clin. Neurol. *146*, 21–32. https://doi.org/10.1016/B978-0-12-804279-3.00002-2.
6. Johanson, C.E., Stopa, E.G., and McMillan, P.N. (2011). The blood-cerebrospinal fluid barrier: structure and functional significance. Methods Mol. Biol. *686*, 101–131. https://doi.org/10.1007/978-1-60761-938-3_4.
7. Khasawneh, A.H., Garling, R.J., and Harris, C.A. (2018). Cerebrospinal fluid circulation: what do we know and how do we know it? Brain Circ. *4*, 14–18. https://doi.org/10.4103/bc.bc_3_18.
8. Cushing, H. (1914). Studies on the cerebro-spinal fluid: I. Introduction. J. Med. Res. *31*, 1–19.
9. Ghersi-Egea, J.F., Strazielle, N., Catala, M., Silva-Vargas, V., Doetsch, F., and Engelhardt, B. (2018). Molecular anatomy and functions of the choroidal blood-cerebrospinal fluid barrier in health and disease. Acta Neuropathol. *135*, 337–361. https://doi.org/10.1007/s00401-018-1807-1.
10. Reese, T.S., and Karnovsky, M.J. (1967). Fine structural localization of a blood-brain barrier to exogenous peroxidase. J. Cell Biol. *34*, 207–217. https://doi.org/10.1083/jcb.34.1.207.
11. Brightman, M.W., and Reese, T.S. (1969). Junctions between intimately apposed cell membranes in the vertebrate brain. J. Cell Biol. *40*, 648–677. https://doi.org/10.1083/jcb.40.3.648.
12. Amtorp, O., and Sorensen, S.C. (1974). The ontogenetic development of concentration differences for protein and ions between plasma and cerebrospinal fluid in rabbits and rats. J. Physiol. *243*, 387–400. https://doi.org/10.1113/jphysiol.1974.sp010759.
13. Nabeshima, S., Reese, T.S., Landis, D.M., and Brightman, M.W. (1975). Junctions in the meninges and marginal glia. J. Comp. Neurol. *164*, 127–169. https://doi.org/10.1002/cne.901640202.
14. La Manno, G., Siletti, K., Furlan, A., Gyllborg, D., Vinsland, E., Mossi Albiach, A., Mattsson Langseth, C., Khven, I., Lederer, A.R., Dratva, L.M., et al. (2021). Molecular architecture of the developing mouse brain. Nature *596*, 92–96. https://doi.org/10.1038/s41586-021-03775-x.
15. Derk, J., Como, C.N., Jones, H.E., Joyce, L.R., Kim, S., Spencer, B.L., Bonney, S., O'Rourke, R., Pawlikowski, B., Doran, K.S., and Siegenthaler, J.A. (2023). Formation and function of the meningeal arachnoid barrier around the developing mouse brain. Dev. Cell *58*, 635–644.e4. https://doi.org/10.1016/j.devcel.2023.03.005.
16. Yamashima, T., Tohma, Y., and Yamashita, J. (1992). Expression of cell adhesion molecule E-cadherin in human arachnoid villi. J. Neurosurg. *77*, 749–756. https://doi.org/10.3171/jns.1992.77.5.0749.
17. Holman, D.W., Grzybowski, D.M., Mehta, B.C., Katz, S.E., and Lubow, M. (2005). Characterization of cytoskeletal and junctional proteins expressed by cells cultured from human arachnoid granulation tissue. Cerebrospinal Fluid Res. *2*, 9. https://doi.org/10.1186/1743-8454-2-9.
18. Hannocks, M.J., Pizzo, M.E., Huppert, J., Deshpande, T., Abbott, N.J., Thorne, R.G., and Sorokin, L. (2018). Molecular characterization of perivascular drainage pathways in the murine brain. J. Cereb. Blood Flow Metab. *38*, 669–686. https://doi.org/10.1177/0271678X17749689.
19. Weed, L.H. (1914). Studies on cerebro-spinal fluid. No. II: The theories of drainage of cerebro-spinal fluid with an analysis of the methods of investigation. J. Med. Res. *31*, 21–49.
20. Andres, K.H. (1967). Uber die Feinstruktur der arachnoidea und dura mater von Mammalia. Z. Zellforsch. MIK Ana *79*, 272–295.
21. Kinaci, A., Bergmann, W., Bleys, R.L., van der Zwan, A., and van Doormaal, T.P. (2020). Histologic comparison of the dura mater among species. Comp. Med. *70*, 170–175. https://doi.org/10.30802/AALAS-CM-19-000022.
22. Schachenmayr, W., and Friede, R.L. (1978). The origin of subdural neomembranes. I. Fine structure of the dura-arachnoid interface in man. Am. J. Pathol. *92*, 53–68.
23. Zhang, E.T., Inman, C.B., and Weller, R.O. (1990). Interrelationships of the pia mater and the perivascular (Virchow-Robin) spaces in the human cerebrum. J. Anat. *170*, 111–123.
24. Vandenabeele, F., Creemers, J., and Lambrichts, I. (1996). Ultrastructure of the human spinal arachnoid mater and dura mater. J. Anat. *189*, 417–430.
25. Roggendorf, W., and Cervós-Navarro, J. (1977). Ultrastructure of arterioles in the cat brain. Cell Tissue Res. *178*, 495–515. https://doi.org/10.1007/BF00219571.
26. Soderblom, C., Luo, X., Blumenthal, E., Bray, E., Lyapichev, K., Ramos, J., Krishnan, V., Lai-Hsu, C., Park, K.K., Tsoulfas, P., and Lee, J.K. (2013). Perivascular fibroblasts form the fibrotic scar after contusive spinal cord injury. J. Neurosci. *33*, 13882–13887. https://doi.org/10.1523/JNEUROSCI.2524-13.2013.
27. Marques, S., Zeisel, A., Codeluppi, S., van Bruggen, D., Mendanha Falcão, A., Xiao, L., Li, H., Häring, M., Hochgerner, H., Romanov, R.A., et al. (2016). Oligodendrocyte heterogeneity in the mouse juvenile and adult central nervous system. Science *352*, 1326–1329. https://doi.org/10.1126/science.aaf6463.
28. Vanlandewijck, M., He, L., Mäe, M.A., Andrae, J., Ando, K., Del Gaudio, F., Nahar, K., Lebouvier, T., Laviña, B., Gouveia, L., et al. (2018). A molecular atlas of cell types and zonation in the brain vasculature. Nature *554*, 475–480. https://doi.org/10.1038/nature25739.
29. Zeisel, A., Hochgerner, H., Lönnerberg, P., Johnsson, A., Memic, F., van der Zwan, J., Häring, M., Braun, E., Borm, L.E., La Manno, G., et al. (2018). Molecular architecture of the mouse nervous system. Cell *174*, 999–1014.e22. https://doi.org/10.1016/j.cell.2018.06.021.
30. Wang, J., Rattner, A., and Nathans, J. (2023). Bacterial meningitis in the early postnatal mouse studied at single-cell resolution. eLife *12*, e86130. https://doi.org/10.7554/eLife.86130.
31. Kaur, C., Rathnasamy, G., and Ling, E.A. (2016). The choroid plexus in healthy and diseased brain. J. Neuropathol. Exp. Neurol. *75*, 198–213. https://doi.org/10.1093/jnen/nlv030.
32. Dani, N., Herbst, R.H., McCabe, C., Green, G.S., Kaiser, K., Head, J.P., Cui, J., Shipley, F.B., Jang, A., Dionne, D., et al. (2021). A cellular and spatial map of the choroid plexus across brain ventricles and ages. Cell *184*, 3056–3074.e21. https://doi.org/10.1016/j.cell.2021.04.003.
33. Pikor, N.B., Astarita, J.L., Summers-Deluca, L., Galicia, G., Qu, J., Ward, L.A., Armstrong, S., Dominguez, C.X., Malhotra, D., Heiden, B., et al. (2015). Integration of Th17- and lymphotoxin-derived signals initiates meningeal-resident stromal cell remodeling to propagate neuroinflammation. Immunity *43*, 1160–1173. https://doi.org/10.1016/j.immuni.2015.11.010.
34. Dorrier, C.E., Aran, D., Haenelt, E.A., Sheehy, R.N., Hoi, K.K., Pintarić, L., Chen, Y., Lizama, C.O., Cautivo, K.M., Weiner, G.A., et al. (2021). CNS fibroblasts form a fibrotic scar in response to immune cell infiltration. Nat. Neurosci. *24*, 234–244. https://doi.org/10.1038/s41593-020-00770-9.

35. Yahn, S.L., Li, J., Goo, I., Gao, H., Brambilla, R., and Lee, J.K. (2020). Fibrotic scar after experimental autoimmune encephalomyelitis inhibits oligodendrocyte differentiation. Neurobiol. Dis. *134*, 104674. https://doi.org/10.1016/j.nbd.2019.104674.

36. Månberg, A., Skene, N., Sanders, F., Trusohamn, M., Remnestål, J., Szczepińska, A., Aksoylu, I.S., Lönnerberg, P., Ebarasi, L., Wouters, S., et al. (2021). Altered perivascular fibroblast activity precedes ALS disease onset. Nat. Med. *27*, 640–646. https://doi.org/10.1038/s41591-021-01295-9.

37. Kelly, K.K., MacPherson, A.M., Grewal, H., Strnad, F., Jones, J.W., Yu, J., Pierzchalski, K., Kane, M.A., Herson, P.S., and Siegenthaler, J.A. (2016). Col1a1+ perivascular cells in the brain are a source of retinoic acid following stroke. BMC Neurosci. *17*, 49. https://doi.org/10.1186/s12868-016-0284-5.

38. Fernández-Klett, F., Potas, J.R., Hilpert, D., Blazej, K., Radke, J., Huck, J., Engel, O., Stenzel, W., Genové, G., and Priller, J. (2013). Early loss of pericytes and perivascular stromal cell-induced scar formation after stroke. J. Cereb. Blood Flow Metab. *33*, 428–439. https://doi.org/10.1038/jcbfm.2012.187.

39. Bolte, A.C., Shapiro, D.A., Dutta, A.B., Ma, W.F., Bruch, K.R., Kovacs, M.A., Royo Marco, A., Ennerfelt, H.E., and Lukens, J.R. (2023). The meningeal transcriptional response to traumatic brain injury and aging. eLife *12*, e81154. https://doi.org/10.7554/eLife.81154.

40. Göritz, C., Dias, D.O., Tomilin, N., Barbacid, M., Shupliakov, O., and Frisén, J. (2011). A pericyte origin of spinal cord scar tissue. Science *333*, 238–242. https://doi.org/10.1126/science.1203165.

41. Dias, D.O., Kim, H., Holl, D., Werne Solnestam, B., Lundeberg, J., Carlén, M., Göritz, C., and Frisén, J. (2018). Reducing pericyte-derived scarring promotes recovery after spinal cord injury. Cell *173*, 153–165.e22. https://doi.org/10.1016/j.cell.2018.02.004.

42. Dias, D.O., Kalkitsas, J., Kelahmetoglu, Y., Estrada, C.P., Tatarishvili, J., Holl, D., Jansson, L., Banitalebi, S., Amiry-Moghaddam, M., Ernst, A., et al. (2021). Pericyte-derived fibrotic scarring is conserved across diverse central nervous system lesions. Nat. Commun. *12*, 5501. https://doi.org/10.1038/s41467-021-25585-5.

43. Saunders, A., Macosko, E.Z., Wysoker, A., Goldman, M., Krienen, F.M., de Rivera, H., Bien, E., Baum, M., Bortolin, L., Wang, S., et al. (2018). Molecular diversity and specializations among the cells of the adult mouse brain. Cell *174*, 1015–1030.e16. https://doi.org/10.1016/j.cell.2018.07.028.

44. Muhl, L., Genové, G., Leptidis, S., Liu, J., He, L., Mocci, G., Sun, Y., Gustafsson, S., Buyandelger, B., Chivukula, I.V., et al. (2020). Single-cell analysis uncovers fibroblast heterogeneity and criteria for fibroblast and mural cell identification and discrimination. Nat. Commun. *11*, 3953. https://doi.org/10.1038/s41467-020-17740-1.

45. Hamilton, T.G., Klinghoffer, R.A., Corrin, P.D., and Soriano, P. (2003). Evolutionary divergence of platelet-derived growth factor alpha receptor signaling mechanisms. Mol. Cell. Biol. *23*, 4013–4025.

46. Holtwick, R., Gotthardt, M., Skryabin, B., Steinmetz, M., Potthast, R., Zetsche, B., Hammer, R.E., Herz, J., and Kuhn, M. (2002). Smooth muscle-selective deletion of guanylyl cyclase-A prevents the acute but not chronic effects of ANP on blood pressure. Proc. Natl. Acad. Sci. USA *99*, 7142–7147. https://doi.org/10.1073/pnas.102650499.

47. Madisen, L., Zwingman, T.A., Sunkin, S.M., Oh, S.W., Zariwala, H.A., Gu, H., Ng, L.L., Palmiter, R.D., Hawrylycz, M.J., Jones, A.R., et al. (2010). A robust and high-throughput Cre reporting and characterization system for the whole mouse brain. Nat. Neurosci. *13*, 133–140. https://doi.org/10.1038/nn.2467.

48. DeSisto, J., O'Rourke, R., Jones, H.E., Pawlikowski, B., Malek, A.D., Bonney, S., Guimiot, F., Jones, K.L., and Siegenthaler, J.A. (2020). Single-cell transcriptomic analyses of the developing meninges reveal meningeal fibroblast diversity and function. Dev. Cell *54*, 43–59.e4. https://doi.org/10.1016/j.devcel.2020.06.009.

49. Armstrong, P.B. (1970). A fine structural study of adhesive cell junctions in heterotypic cell aggregates. J. Cell Biol. *47*, 197–210. https://doi.org/10.1083/jcb.47.1.197.

50. Haines, D.E. (1991). On the question of a subdural space. Anat. Rec. *230*, 3–21. https://doi.org/10.1002/ar.1092300103.

51. Pease, D.C., and Schultz, R.L. (1958). Electron microscopy of rat cranial meninges. Am. J. Anat. *102*, 301–321. https://doi.org/10.1002/aja.1001020207.

52. Yasuda, K., Cline, C., Vogel, P., Onciu, M., Fatima, S., Sorrentino, B.P., Thirumaran, R.K., Ekins, S., Urade, Y., Fujimori, K., and Schuetz, E.G. (2013). Drug transporters on arachnoid barrier cells contribute to the blood-cerebrospinal fluid barrier. Drug Metab. Dispos. *41*, 923–931. https://doi.org/10.1124/dmd.112.050344.

53. Møllgård, K., Beinlich, F.R.M., Kusk, P., Miyakoshi, L.M., Delle, C., Plá, V., Hauglund, N.L., Esmail, T., Rasmussen, M.K., Gomolka, R.S., et al. (2023). A mesothelium divides the subarachnoid space into functional compartments. Science *379*, 84–88. https://doi.org/10.1126/science.adc8810.

54. Castro Dias, M., Mapunda, J.A., Vladymyrov, M., and Engelhardt, B. (2019). Structure and junctional complexes of endothelial, epithelial and glial brain barriers. Int. J. Mol. Sci. *20*, 5372. https://doi.org/10.3390/ijms20215372.

55. Krisch, B., Leonhardt, H., and Oksche, A. (1983). The meningeal compartments of the median eminence and the cortex. A comparative analysis in the rat. Cell Tissue Res. *228*, 597–640. https://doi.org/10.1007/BF00211479.

56. Balin, B.J., Broadwell, R.D., Salcman, M., and El-Kalliny, M. (1986). Avenues for entry of peripherally administered protein to the central nervous system in mouse, rat, and squirrel monkey. J. Comp. Neurol. *251*, 260–280. https://doi.org/10.1002/cne.902510209.

57. Brøchner, C.B., Holst, C.B., and Møllgård, K. (2015). Outer brain barriers in rat and human development. Front. Neurosci. *9*, 75. https://doi.org/10.3389/fnins.2015.00075.

58. Mariano, C., Sasaki, H., Brites, D., and Brito, M.A. (2011). A look at tricellulin and its role in tight junction formation and maintenance. Eur. J. Cell Biol. *90*, 787–796. https://doi.org/10.1016/j.ejcb.2011.06.005.

59. Iwamoto, N., Higashi, T., and Furuse, M. (2014). Localization of angulin-1/LSR and tricellulin at tricellular contacts of brain and retinal endothelial cells in vivo. Cell Struct. Funct. *39*, 1–8. https://doi.org/10.1247/csf.13015.

60. Russ, D.E., Cross, R.B.P., Li, L., Koch, S.C., Matson, K.J.E., Yadav, A., Alkaslasi, M.R., Lee, D.I., Le Pichon, C.E., Menon, V., and Levine, A.J. (2021). A harmonized atlas of mouse spinal cord cell types and their spatial organization. Nat. Commun. *12*, 5722. https://doi.org/10.1038/s41467-021-25125-1.

61. Yadav, A., Matson, K.J.E., Li, L., Hua, I., Petrescu, J., Kang, K., Alkaslasi, M.R., Lee, D.I., Hasan, S., Galuta, A., et al. (2023). A cellular taxonomy of the adult human spinal cord. Neuron *111*, 328–344.e7. https://doi.org/10.1016/j.neuron.2023.01.007.

62. Gerber, D., Pereira, J.A., Gerber, J., Tan, G., Dimitrieva, S., Yángüez, E., and Suter, U. (2021). Transcriptional profiling of mouse peripheral nerves to the single-cell level to build a sciatic nerve Atlas (SNAT). eLife *10*, e58591. https://doi.org/10.7554/eLife.58591.

63. Thelin, E.P., Frostell, A., Mulder, J., Mitsios, N., Damberg, P., Aski, S.N., Risling, M., Svensson, M., Morganti-Kossmann, M.C., and Bellander, B.M. (2016). Lesion size is exacerbated in hypoxic rats whereas hypoxia-inducible factor-1 alpha and vascular endothelial growth factor increase in injured normoxic rats: A prospective cohort study of secondary hypoxia in focal traumatic brain injury. Front. Neurol. *7*, 23. https://doi.org/10.3389/fneur.2016.00023.

64. Lindblad, C., and Thelin, E.P. (2019). Secondary insults in experimental traumatic brain injury: the addition of hypoxia. In Animal Models of Neurotrauma (Springer), pp. 223–242.

65. Edward Dixon, C.E., Clifton, G.L., Lighthall, J.W., Yaghmai, A.A., and Hayes, R.L. (1991). A controlled cortical impact model of traumatic brain

injury in the rat. J. Neurosci. Methods *39*, 253–262. https://doi.org/10.1016/0165-0270(91)90104-8.

66. Lighthall, J.W. (1988). Controlled cortical impact: a new experimental brain injury model. J. Neurotrauma *5*, 1–15. https://doi.org/10.1089/neu.1988.5.1.
67. Yu, S., Kaneko, Y., Bae, E., Stahl, C.E., Wang, Y., van Loveren, H., Sanberg, P.R., and Borlongan, C.V. (2009). Severity of controlled cortical impact traumatic brain injury in rats and mice dictates degree of behavioral deficits. Brain Res. *1287*, 157–163. https://doi.org/10.1016/j.brainres.2009.06.067.
68. Bajénoff, M., Egen, J.G., Koo, L.Y., Laugier, J.P., Brau, F., Glaichenhaus, N., and Germain, R.N. (2006). Stromal cell networks regulate lymphocyte entry, migration, and territoriality in lymph nodes. Immunity *25*, 989–1001. https://doi.org/10.1016/j.immuni.2006.10.011.
69. Magliozzi, R., Howell, O., Vora, A., Serafini, B., Nicholas, R., Puopolo, M., Reynolds, R., and Aloisi, F. (2007). Meningeal B-cell follicles in secondary progressive multiple sclerosis associate with early onset of disease and severe cortical pathology. Brain *130*, 1089–1104. https://doi.org/10.1093/brain/awm038.
70. Rustenhoven, J., Drieu, A., Mamuladze, T., de Lima, K.A., Dykstra, T., Wall, M., Papadopoulos, Z., Kanamori, M., Salvador, A.F., Baker, W., et al. (2021). Functional characterization of the dural sinuses as a neuroimmune interface. Cell *184*, 1000–1016.e27. https://doi.org/10.1016/j.cell.2020.12.040.
71. Bonney, S.K., Sullivan, L.T., Cherry, T.J., Daneman, R., and Shih, A.Y. (2022). Distinct features of brain perivascular fibroblasts and mural cells revealed by in vivo two-photon imaging. J. Cereb. Blood Flow Metab. *42*, 966–978. https://doi.org/10.1177/0271678X211068528.
72. Mestre, H., Verma, N., Greene, T.D., Lin, L.A., Ladron-de-Guevara, A., Sweeney, A.M., Liu, G., Thomas, V.K., Galloway, C.A., de Mesy Bentley, K.L., et al. (2022). Periarteriolar spaces modulate cerebrospinal fluid transport into brain and demonstrate altered morphology in aging and Alzheimer's disease. Nat. Commun. *13*, 3897. https://doi.org/10.1038/s41467-022-31257-9.
73. Schiavinato, A., Przyklenk, M., Kobbe, B., Paulsson, M., and Wagener, R. (2021). Collagen type VI is the antigen recognized by the ER-TR7 antibody. Eur. J. Immunol. *51*, 2345–2347. https://doi.org/10.1002/eji.202149263.
74. Waggener, J.D., and Beggs, J. (1967). The membranous coverings of neural tissues: an electron microscopy study. J. Neuropathol. Exp. Neurol. *26*, 412–426. https://doi.org/10.1097/00005072-196707000-00005.
75. Rascol, M.M., and Izard, J.Y. (1976). The subdural neurothelium of the cranial meninges in man. Anat. Rec. *186*, 429–436. https://doi.org/10.1002/ar.1091860308.
76. Frederickson, R.G. (1991). The subdural space interpreted as a cellular layer of meninges. Anat. Rec. *230*, 38–51. https://doi.org/10.1002/ar.1092300105.
77. Haines, D.E., Harkey, H.L., and al-Mefty, O. (1993). The "subdural" space: a new look at an outdated concept. Neurosurgery *32*, 111–120. https://doi.org/10.1227/00006123-199301000-00017.
78. Mack, J., Squier, W., and Eastman, J.T. (2009). Anatomy and development of the meninges: implications for subdural collections and CSF circulation. Pediatr. Radiol. *39*, 200–210. https://doi.org/10.1007/s00247-008-1084-6.
79. Derk, J., Jones, H.E., Como, C., Pawlikowski, B., and Siegenthaler, J.A. (2021). Living on the edge of the CNS: meninges cell diversity in health and disease. Front. Cell. Neurosci. *15*, 703944. https://doi.org/10.3389/fncel.2021.703944.
80. Sorokin, L.M., Conzelmann, S., Ekblom, P., Battaglia, C., Aumailley, M., and Timpl, R. (1992). Monoclonal antibodies against laminin A chain fragment E3 and their effects on binding to cells and proteoglycan and on kidney development. Exp. Cell Res. *201*, 137–144. https://doi.org/10.1016/0014-4827(92)90357-e.
81. He, L., Vanlandewijck, M., Mäe, M.A., Andrae, J., Ando, K., Del Gaudio, F., Nahar, K., Lebouvier, T., Laviña, B., Gouveia, L., et al. (2018). Single-cell RNA sequencing of mouse brain and lung vascular and vessel-associated cell types. Sci. Data *5*, 180160. https://doi.org/10.1038/sdata.2018.160.
82. Choi, I., Chung, H.K., Ramu, S., Lee, H.N., Kim, K.E., Lee, S., Yoo, J., Choi, D., Lee, Y.S., Aguilar, B., and Hong, Y.K. (2011). Visualization of lymphatic vessels by Prox1-promoter directed GFP reporter in a bacterial artificial chromosome-based transgenic mouse. Blood *117*, 362–365. https://doi.org/10.1182/blood-2010-07-298562.
83. Ortsäter, H., Hernández-Vásquez, M.N., Ulvmar, M.H., Gow, A., and Mäkinen, T. (2021). An inducible Cldn11-CreER(T2) mouse line for selective targeting of lymphatic valves. Genesis *59*, e23439. https://doi.org/10.1002/dvg.23439.
84. Satija, R., Farrell, J.A., Gennert, D., Schier, A.F., and Regev, A. (2015). Spatial reconstruction of single-cell gene expression data. Nat. Biotechnol. *33*, 495–502. https://doi.org/10.1038/nbt.3192.
85. Kim, D., Pertea, G., Trapnell, C., Pimentel, H., Kelley, R., and Salzberg, S.L. (2013). TopHat2: accurate alignment of transcriptomes in the presence of insertions, deletions and gene fusions. Genome Biol. *14*, R36. https://doi.org/10.1186/gb-2013-14-4-r36.
86. Liao, Y., Smyth, G.K., and Shi, W. (2014). featureCounts: an efficient general purpose program for assigning sequence reads to genomic features. Bioinformatics *30*, 923–930. https://doi.org/10.1093/bioinformatics/btt656.
87. Macosko, E.Z., Basu, A., Satija, R., Nemesh, J., Shekhar, K., Goldman, M., Tirosh, I., Bialas, A.R., Kamitaki, N., Martersteck, E.M., et al. (2015). Highly parallel genome-wide expression profiling of individual cells using nanoliter droplets. Cell *161*, 1202–1214. https://doi.org/10.1016/j.cell.2015.05.002.
88. Picelli, S., Faridani, O.R., Björklund, A.K., Winberg, G., Sagasser, S., and Sandberg, R. (2014). Full-length RNA-seq from single cells using Smart-seq2. Nat. Protoc. *9*, 171–181. https://doi.org/10.1038/nprot.2014.006.
89. Bjørnholm, K.D., Del Gaudio, F., Li, H., Li, W., Vazquez-Liebanas, E., Mäe, M.A., Lendahl, U., Betsholtz, C., Nilsson, P., Karlström, H., and Vanlandewijck, M. (2023). A robust and efficient microvascular isolation method for multimodal characterization of the mouse brain vasculature. Cell Rep. Methods *3*, 100431. https://doi.org/10.1016/j.crmeth.2023.100431.

Neuron
NeuroResource

CellPress
OPEN ACCESS

STAR★METHODS

KEY RESOURCES TABLE

REAGENT or RESOURCE	SOURCE	IDENTIFIER
Antibodies		
rabbit-anti-AQP4	Millipore	Cat# AB2218; RRID: AB_1163383
mouse-anti-αSMA-647	Santa Cruz	Cat# sc32251; RRID: AB_262054
goat-anti Cd144	Cell Signaling	Cat# AF1002; RRID: AB_2077789
rat anti- Cd144	BD Biosciences	Cat# 555289; RRID: AB_395707
goat-anti-CD31	R&D Systems	Cat# AF3628; RRID: AB_2161028
rat-anti-CD31	BD Biosciences	Cat# 553370; RRID: AB_394816
rabbit-anti-Cdh1	Cell Signaling Technology	Cat# 31956; RRID: AB_2291471
goat-anti-Cdh1	R&D Systems	Cat# AF748 RRID: AB_355568
rabbit anti-Cldn11	Thermo Fisher Scientific	Cat# 36-4500; RRID: AB_2533259
rabbit anti-Crapb2	Proteintech	Cat# 10225-1-AP; RRID: AB_2085455
goat-anti-Dpp4	R&D Systems	Cat# AF954; RRID: AB_355739
rat-anti-Emcn	Abcam	Cat# ab106100; RRID: AB_10859306
chicken-anti-GFP	Abcam	Cat# ab13970; RRID: AB_300798
rat-anti-mouse-Lama1	Sorokin et al.[80] a gift from L. Sorokin	N/A
rabbit-anti-mouse Lama1	Hannocks et al.[18] a gift from L. Sorokin	N/A
rat anti-Angulin1/LSR	Iwamoto et al.[59] a gift from M. Furuse	N/A
rat-anti-RFP	ChromoTec	Cat# 5F8; RRID: 2336064
Rabbit-anti-SLC16a1	Origene	Cat# TA321556;
rabbit- anti vWF	Agilent	Cat# A0082; RRID: AB_2315602
Chemicals, peptides, and recombinant proteins		
TSA Plus Fluorescein Reagent	Akoya Biosciences	Cat# NEL741E001KT
TSA Plus Cy3 Reagent	Akoya Biosciences	Cat# NEL744E001KT
TSA Plus Cy5 Reagent	Akoya Biosciences	Cat# NEL745E001KT
Osteosoft	Sigma Aldrich	Cat# 1.01728
Critical commercial assays		
Chromium Next GEM Single Cell 3' GEM, Library & Gel Bead Kit v3.1 16 rxns	10X Genomics	Cat# 1000121
Chromium Next GEM Chip G Single Cell Kit, 48 rxns	10X Genomics	Cat# 1000120
RNAscope® Multiplex Fluorescent Reagent Kit v2	Advanced Cell Diagnostics	Cat# 323110
Deposited data		
Raw sequencing reads and processed gene expression counts	This paper	GEO: GSE227713, GSE228882, GSE233270

(*Continued on next page*)

Please cite this article in press as: Pietilä et al., Molecular anatomy of adult mouse leptomeninges, Neuron (2023), https://doi.org/10.1016/j.neuron.2023.09.002

Continued

REAGENT or RESOURCE	SOURCE	IDENTIFIER
Raw sequencing reads and processed gene expression counts	He et al.[81]	GEO: GSE98816
Experimental models: Organisms/strains		
Mouse: C57BL/6J	The Jackson Laboratory	JAX: 000664
Mouse: *Pdgfra*$^{tm11(EGFP)Sor}$	Hamilton et al.[45] a gift from P. Soriano	RRID: IMSR_JAX:007669
Mouse: *Tg(Pdgfra-EGFP)NW179Gsat/Mmucd*	Gensat.org	RRID: MMRRC_034352-UCD
Mouse: Tg(Prox1-EGFP)KY221Gsat	Choi et al.[82] a gift from M. Ulvmar	MGI: 4847348
Mouse: *Gt(ROSA)26Sor*$^{tm14(CAG-tdTomato)Hze}$	Madisen et al.[47]	RRID: IMSR_JAX:007914
Mouse: Tg(Tagln-cre)1Her/J	Holtwick et al.[46]	RRID: IMSR_JAX:004746
Mouse: *Tg(Lum-creERT2)*	This paper	N/A
Mouse: *Tcf21*^{P2ACreERT2}	This paper	N/A
Mouse: Tg(Cldn11-creERT2)	Ortsäter et al.[83]	N/A
Oligonucleotides		
RNAscope probe: Mm-Crabp2	Advanced Cell Diagnostics	Cat# 583461-C3
RNAscope probe: Mm-Col12a1	Advanced Cell Diagnostics	Cat# 312631
RNAscope probe: Mm-Col15a1	Advanced Cell Diagnostics	Cat# 1092391-C2
RNAscope probe: Mm-Dpep1	Advanced Cell Diagnostics	Cat# 480831-C3
RNAscope probe: Mm-Dpp4	Advanced Cell Diagnostics	Cat# 412571_C3
RNAscope probe: Mm-Fmod	Advanced Cell Diagnostics	Cat# 479421; Cat#479421-C2
RNAscope probe: Mm-Lama1	Advanced Cell Diagnostics	Cat# 494931
RNAscope probe: Mm-Moxd1	Advanced Cell Diagnostics	Cat# 497531-C3
RNAscope probe: Mm-Pdgfra	Advanced Cell Diagnostics	Cat# 518041; Cat# 518041-C2
RNAscope probe: Mm-Pecam1	Advanced Cell Diagnostics	Cat# 316721; Cat# 316721-C3
RNAscope probe: Mm-Ppp1r1a	Advanced Cell Diagnostics	Cat# 492601
RNAscope probe: Mm-Sidt1	Advanced Cell Diagnostics	Cat# 425471-C3
RNAscope probe: Mm-Slc7a11	Advanced Cell Diagnostics	Cat# 422511-C2
RNAscope probe: Mm-Slc7a14	Advanced Cell Diagnostics	Cat# 544781-C2
RNAscope probe: Mm-Slc22a2	Advanced Cell Diagnostics	Cat# 513071
RNAscope probe: Mm-Slc47a1	Advanced Cell Diagnostics	Cat# 513101
Software and algorithms		
CellRanger (5 and 6)	10X Genomics	https://support.10xgenomics.com
R package Seurat (3.1.1; 4.0.2)	Satija et al.[84]	https://satijalab.org/seurat/index.html
Tophat (2.1.1)	Kim et al.[85]	https://ccb.jhu.edu/software/tophat/index.shtml
Subread (1.4.6-p5)	Liao et al.[86]	https://subread.sourceforge.net/
R (3.5.1; 4.2.1)	The R Foundation	https://www.r-project.org
ggplot2 (3.2.1)	The R Foundation	https://cran.r-project.org/web/packages/ggplot2/index.html
R package GOstat (2.48.0)	Bioconductor	https://bioconductor.org/packages/release/bioc/html/GOstats.html
R packages GO.db (3.6.0)	Bioconductor	https://bioconductor.org/packages/release/data/annotation/html/GO.db.html
FIJI	Open source	https://imagej.nih.gov/ij/ RRID: SCR_003070

(*Continued on next page*)

Please cite this article in press as: Pietilä et al., Molecular anatomy of adult mouse leptomeninges, Neuron (2023), https://doi.org/10.1016/j.neuron.2023.09.002

Continued

REAGENT or RESOURCE	SOURCE	IDENTIFIER
LAS X software (3.5.723225)	Leica	https://www.leica-microsystems.com/products/microscope-software/p/leica-las-x-ls/downloads/
Other		
Online database: Adult leptomeningeal droplet scRNASeq data	This paper	http://betsholtzlab.org/Publications/BrainFB/meninges/database.html
Online database: Adult dural droplet scRNASeq data	This paper	http://betsholtzlab.org/Publications/BrainFB/dural/database.html
Online database: Adult brain vascular fragment droplet ScRNASeq data	This paper	http://betsholtzlab.org/Publications/BrainFB/VascularStubs/database.html
Online database: Adult brain FACS-SmartSeq2 data	This paper	http://betsholtzlab.org/Publications/MouseBrainFB/search.html
Online database: Adolescent brain fibroblast droplet scRNASeq data	Zeisel et al.[29]	http://betsholtzlab.org/Publications/BrainFB/Adolescent/FB.html
Online database: Embryonic brain fibroblast droplet scRNASeq data	La Manno et al.[14]	http://betsholtzlab.org/Publications/BrainFB/Dev/search.html

RESOURCE AVAILABILITY

Lead contact

Further information and requests for resources should be directed to the lead contact, Christer Betsholtz (christer.betsholtz@igp.uu.se).

Materials availability

Mouse lines generated in this study are available from the lead contact upon request.

Data and code availability

- Single-cell RNA-seq data have been deposited at GEO and are publicly available as of the date of publication. Accession numbers are listed in the key resources table. Online searchable databases of annotated gene expression data are described in the key resources table.
- This paper does not report any original code.
- All data and additional information required to re-analyze the data reported in this paper are available from the lead contact upon request.

EXPERIMENTAL MODEL AND SUBJECT DETAILS

Animals

All mouse experiments were conducted according to Swedish and European legislation. Ethical permits were approved by the Animal Ethics Committees in Uppsala (C115/15, 5.8.18-03029/2020) and in Stockholm (5253-2019, 1835-2021). Experimental procedures were performed under anesthesia and all efforts were made to minimize suffering. Animals were housed on a 12h light-dark cycle, with *ad libitum* access to water and standard chow.

Both sexes were used for scRNAseq experiments. The sex of individual single-cell transcriptomes is accessible through online database search for female-specific X chromosome-encoded mRNAs, e.g. *Xist* and *Tsix*, and male-specific Y chromosome-encoded mRNAs, e.g. *Kdm5d* and *Ddx3y*. Male and female cells showed limited skewing in UMAP distribution, suggesting minor (or no), influence of sex on autosomal gene transcription. However, the experiments were not designed for the purpose of revealing such differences, and the results should therefore not be taken as evidence for their absence.

For the *in situ* analyses of mRNA, protein and reporter expression, both sexes were used in all analyses, except the TBI injury model, where only males were used, in order to conform with earlier applications of the method.[63–67] We did not observe sex-specific differences in these results, but again, these analyses were not designed for the purpose of revealing putative sex-specific differences in meningeal anatomy and do therefore not allow firm conclusions about their possible existence.

For all experiments, mice and mouse strains listed below, analyses were done using adult mice within the age span 2-14 months, except for scRNAseq approach 3 (see below), for which the age span was 3-24 months.

Wild-type C57BL6/J mice (JAX 00064), and the following genetically modified mice were used: *Pdgfra*-H2BGFP knock-in reporter mouse (*Pdgfra*$^{tm11(EGFP)Sor}$)[45]; *Pdgfra*-eGF BAC transgenic reporter mouse (Tg(Pdgfra-EGFP)NW179Gsat/Mmucd, obtained from Gensat.org); Ai14 conditional tdTomato reporter mouse (Gt(ROSA)26Sor$^{tm14(CAG-tdTomato)Hze}$)[47]; *SM22*-Cre mouse (Tg(Tagln-cre) 1Her/J),[46] *Prox1*-EGFP mouse (Tg(Prox1-EGFP)KY221Gsat)[82]; *Cldn1*-CreERT2 mouse (Tg(Cldn11-cre/ERT2)151Tmak)[83]; *Lum*-CreERT2 mouse and *Tcf21*-P2ACreERT2 mouse (see below). All mice were backcrossed on a C57BL6/J genetic background. Tg(*Lum*-CreERT2) were generated (by Taconic Biosciences, Denmark) through pronuclear injection of a BAC clone containing the entire *Lum* gene, and where the endogenous translation initiation codon from the *Lum* gene was used to drive expression of CreERT2. The coding sequence in exon 2, as well as the splice donor site at the junction between exon 2 and intron 2 (50bp), was replaced with a cassette containing the open reading frame for CreERT2 and the *Lum* 3′ untranslated region (UTR). A hGHpA (human Growth Hormone) polyadenylation signal was inserted 3' of the *Lum* 3'UTR. The mouse genomic sequence downstream of the intron 2 was left intact in order to preserve all potential regulatory elements driving the expression of the *Lum* gene present in this intron. *Tcf21*-P2ACreERT2 mice were generated by insertion of a cDNA cassette encoding a V5-bio epitope tag, a P2A sequence, and CreERT2 immediately 5'of the endogenous stop codon of the *Tcf21* gene in ES cells through homologous recombination, blastocyst injection and germline transmission (Cyagen, Santa Clara, CA). *SM22*-Cre, *Cldn11*-CreERT2, Tg(*Lum*-creERT2) and *Tcf21*-P2ACreERT2 mice, respectively, were crossed with Ai14 reporter mice (Gt(ROSA)26Sor$^{tm14(CAG-tdTomato)Hze}$) to generate *SM22*-Cre; Ai14, *Cldn11*-CreERT2; Ai14, *Lum*-creERT2; Ai14 and *Tcf21*-P2ACreERT2:Ai14 mice. Cre-mediated recombination in adult (2-6 months old) mice was induced by 3 to 5 consecutive administrations by oral gavage of 1-2 mg of Tamoxifen (T5648, Sigma-Aldrich) dissolved in peanut oil (10 or 20 mg/ml, P2144, Sigma-Aldrich).

METHOD DETAILS

Isolation of cells and scRNAseq

We used four separate approaches to isolate cells (approaches 1-4) and two different methods for scRNAseq (Droplet-based scRNA-seq[87] and SmartSeq2[88]), which were applied to cells isolated using approaches 1-3 and 4, respectively. Droplet scRNAseq was performed using the 10x Genomics Gene Expression kit v3.1 and a Chromium controller (10x Genomics) according to the manufacturer's recommendation. For SmartSeq2, we followed a previously described protocol.[81]

In approach 1, the calvarium was removed to expose the leptomeninges, which were carefully peeled off from cerebral hemispheres of three months old *Pdgfra-H2BGFP*, n=5 males and n=2 females using forceps and transferred to an Eppendorf tube with 400 μl ice-cold DMEM. Next, 100 μl of ice-cold DMEM with 0.01 mg/ml Collagenase type 2 (Sigma, C6885) was added to the tube, for a final concentration of 0.002 mg/ml Collagenase type 2 in 500 μl of DMEM. Next, the solution was incubated for 5 min at 37 °C with slow rotation. Tissue digests were carefully aspirated up and down for 10 times though a 20G syringe and further incubated for 5 min at slow rotation in 37 °C. Cells were pelleted at 300g for 5 min at 4°C and dissolved in FACS buffer (DMEM without phenol red, 2%& Fetal Bovine Serum, 1 mM EDTA pH 8.0). The cells were counted on a LUNA-FL Dual Fluorescence Cell Counter (LogosBio) and loaded on a 10x Genomics Chromium controller, aiming for a maximal recovery of 5000 cells per sample. Of the total of 4,862 single-cell transcriptomes, vascular cells, immune cells, and stromal cells were the most abundant cells identified (Figures 1C and S1A).

In approach 2, females (N=3) and a male (n=1) were given a lethal dose of ketamine and xylazine and perfused through the left ventricle with ice-cold phosphate-buffered saline (PBS) for 3 min with a rate of 8 ml/min after puncture of the right auricle. Head dissection was done by insertion of a fine pair of scissors to the cisterna magna and by cutting along the lines of the parietal bone until the rostral part was reached on both sides. The dorsal calvarium (skull cup) was then removed carefully, taking extra care not to harm the attached dura mater. The dura mater was carefully detached from the dorsal skull bone by peeling it off in one piece using forceps under a dissection microscope and placed into ice-cold HBSS without Ca^{2+} and Mg^{2}. Dura mater from four mice per group were moved into 500 μl DPBS with 0.5% BSA and cut into small pieces with fine scissors. Another 500 μl of DPBS with 0.5% BSA with 3 μl of DNase I (Sigma#C2139, stock 100 mg/ml, working concentration 0.2 mg/ml) and 2 μl of Collagenase VIII (Sigma#C2139, stock 100 mg/ml, working concentration 0.2 mg/ml) was added into each tube. Samples were digested at 37 °C incubator with rotation speed 20 cycles/min (10+10 min for meninges) and mixed with 1 ml pipette in the middle and at the end of incubation. After transfer of digestion mixture into a 12 ml of ice-cold HBSS without Ca2+ and Mg2+, samples were filtered through 70 um cell strainer and centrifuged at 4 °C, 300g for 7 min, resuspended with 500ul of PBS and finally filtered through blue strainer cap (cat# 352235, Life Sciences) into a FACS tube (cat#352053, Life Sciences). DAPI (1:1000) was added right before sorting and DAPI negative single cells were sorted with BD influx into an Eppendorf DNA LoBind tube loaded with 10 μl of PBS with 0.04 % BSA. After cell sorting, additional BSA was added to get final concentration of BSA to be at least 0.04 %. The cells were centrifuged at 4 °C, 300g for 7 min and resuspended to optimal cell concentration for 10X library preparation. Library was prepared from the samples. This procedure yielded a total of 28,352 single-cell transcriptomes, most of which corresponded to immune cells. Of this total, 4,061 transcriptomes were judged to represent fibroblasts, including a small cluster of osteoblasts (expressing e.g., *Bglap* (osteocalcin) and *Sparc* (osteonectin), presumably originating from the inner surface of the skull (Figure S2A). We also found transcriptomes corresponding to vascular cells and small numbers of pinealocytes (e.g., *Pax6*), habenula neurons (e.g., *Pde6g* and *Tph1*), and choroid plexus epithelial cells (expressing e.g., *Ttr* and *Foxj1*). The presence of the latter likely reflects dural attachment to the pineal gland and the third ventricle.

In approach 3, vascular fragments were isolated from whole mouse brain except the olfactory bulb using a CD31-panning protocol and digested into cell suspensions as described[89] and single cell libraries were prepared by the 10x Genomics Gene Expression kit v3.1. For this approach, five age groups of male and female C57Bl6/J mice were used (3, 6, 9, 12 and 24 months old) with n=3 mice per group, n=15 mice in total. Most of the total of 272,443 single-cell transcriptomes were identified as vascular cells and microglia, but the population also included 173 fibroblast transcriptomes (≈ 0.05%) (Figures 1C and S3).

In approach 4, we enriched for fibroblasts more specifically and provided deeper transcriptomic information per cell using fluorescence-activated cell sorting (FACS) from two reporter mouse strains: *Pdgfra*-H2BGFP[45] and *Tagln-CreERT2:Ai14*[46,47] known to label fibroblasts, vascular mural cells, and astrocytes[28,81] (Figure 1B) and scRNAseq by SmartSeq2.[88] Brain tissue from both males (n=8) and females (n=2) were mechanically and enzymatically digested and vascular fragments isolated using CD31 antibody coated Dynabeads and further digested into cell suspension. This approach yielded transcriptomes from 234 fibroblasts, along with other vascular and glial cells (Figures 1C and S4).

Single-cell RNA sequencing data analysis

Droplet based libraries were generated per manufacturer's recommendation and sequenced on an Illumina NextSeq 2000 P2 or P3 100 cycles flow cell, aiming for a minimum of 35.000 reads per cell. After sequencing, the data was demultiplexed and aligned against the *Mus Musculus* mm10 genome using 10x Genomics CellRanger version 5 and 6. The SmartSeq2 libraries were prepared and sequenced were performed as described previously.[81] Reads were aligned to the mouse reference genome (mm10) with tophat (version 2.1.1),[85] and the raw read counts for each gene were summarized using featureCounts function from the Subread package (version 1.4.6-p5).[86] Newly obtained scRNAseq data analyzed in this study can be accessed using the following GEO database numbers: GEO: GSE227713, GSE228882, GSE233270. Access to processed data is provided at http://betsholtzlab.org/Publications/BrainFB/Data/BFBdata.html.

The raw counts data for each dataset were then respectively loaded in R Seurat packages (version: 3.1.1; 4.0.2) for quality control, filtering, normalization, clustering, differential expression analysis and further downstream analysis.[84] For the dissected leptomeningeal data, cells with less than 500 genes or with mitochondrial gene percentage higher than 10% were filtered out. A scale factor of 10,000 was used to normalize each cell. The top 2000 variable genes were identified using the vst method in FindVariableFeatures function in Seurat package. The specific lists of the top 2,000 variable genes for the four datasets are listed in Table S3. These variable genes were then used for principal component analysis in RunPCA function, and the first 30 principal components were used for dimension reduction analysis with Uniform Manifold Approximation and Projection (UMAP) method, and also in the shared nearest neighbor clustering analysis in FindNeighbors function. The clustering resolution were set at 0.5 in FindClusters function. To identify the marker/enriched genes for each cluster, the FindAllMarkers function was used and a Wilcoxon Rank Sum test was applied to identify the differentially expressed genes between groups. The default fold change cut-off 0.25 (log) and bonferroni multiple test corrected p value = 0.05 were set as the significance cut-off. For the other 10x Genomics datasets, same approaches were applied as for the leptomeningeal data. For visualization, the UMAP views were plotted using the DimPlot function in Seurat. The marker expression in dot plots were visualized using DotPlot function, and the heat maps were generated using DoHeatmap function in Seurat. To visualize the expression in each individual cell, the bar plot method and the database constructions were implemented as described previously.[81] To identify the functional enrichment, the GO analysis was performed in R software using GOstat packages (version 2.48.0) and GO.db (version 3.6.0). The statistics p value = 0.001 was set as the significance cut-off.

Immunostaining of tissue sections

Mice of both sexes (2-6 months) were perfused through the heart with Hank's Balanced Salt Solution (HBSS, Gibco) followed by 4% buffered formaldehyde (Histolab Products AB). Brains were dissected out, postfixed in 4% PFA at +4 °C for 4h and washed in PBS. Coronal vibratome sections (75-100μm) were incubated in blocking/permeabilization solution (1% bovine serum albumin, 0.5% Triton X-100 in PBS) at 4 °C overnight, followed by primary antibody solution (0.5% bovine serum albumin, 0.25% Triton X-100 in PBS) at 4 °C for two nights, 3 x washes in PBS and finally secondary antibody solution overnight. For nuclear staining, sections were incubated with Hoechst 33342 (1:5000, Invitrogen) before mounting in ProLong Gold Antifade (Life Technologies).

For spinal cord immunofluorescence, spines were dissected from thoracic, or lumbar area after perfusion fixation and post-fixation as above, cleaned from tissue, incubated in decalcification solution for 48h at RT on a shaker (Osteosoft, Sigma Aldrich), washed with PBS and incubated in 30% sucrose (in PBS) for 24-48h and snap frozen in embedding medium (NEG-50™, Richard Allan Scientific). 10 μm transverse cryosections were washed twice with PBS, incubated 3h at RT in blocking/ permeabilization solution (0.3% Triton X-100 in protein block solution, Dako X0909), followed by primary antibody solution (in PBS) for overnight at 4 °C, 3x washes in PBS and 2h incubation at RT with secondary antibody solution (in PBS). For nuclear staining, Hoechst 33342 (1:10 000, Invitrogen) was added to one PBS wash before mounting in ProLong Gold Antifade (Life Technologies).

For brain *en face* immunofluorescence, 200-400 μm transversal vibratome sections from the surface of the dorsal cerebrum were prepared and stained as described above, except for those mouse brains used for immunofluorescence of junctional proteins (LSR, CLDN11 and CDH1). The mice used for immunofluorescence of junctional proteins were perfused with HBSS followed by 1% PFA and after dissection they were post-fixed in ice-cold 100% methanol (VWR) for 4 h. Rehydration of the brains was performed with a series of incubations of 10-15 min in 85% Methanol, 50% Methanol, 25% Methanol and finally in PBS prior vibratome sectioning.

Please cite this article in press as: Pietilä et al., Molecular anatomy of adult mouse leptomeninges, Neuron (2023), https://doi.org/10.1016/j.neuron.2023.09.002

Primary antibodies used: rat-anti-mouse-Lama1[80] (#200, conditioned medium) and rabbit-anti-mouse Lama1[18] (1:600, #317) kind gifts from Prof. Lydia Sorokin; rabbit-anti-Cdh1 (1:200, Cell Signalling, 31956); goat-anti-Cdh1 (1:100, R&D Systems, AF748), rat-anti-RFP (1:200, ChromoTec, 5F8); chicken-anti-GFP (1:200, Abcam, ab13970); goat-anti-Dpp4 (1:200, R&D Systems, AF954); rabbit-anti-AQP4 (1:200, Millipore, AB2218); goat-anti-CD31 (1:200, R&D Systems, AF3628); mouse-anti-ASMA direct-conjugated to A647 (1:100 Santa Cruz, sc32251); rat-anti-Angulin/LSR (1:20, a gift from M. Furuse); rabbit anti-Cldn11 (1:100, Thermo Fisher Scientific, 36–4500); rabbit-anti-Crapb2 (1:100, ProteinTech, 10225–1-AP); rat-anti-Emcn (1:200, Abcam, AB106100) and anti-Slc16a1 (1:100, Origene, TA321556) antibody. Donkey secondary antibodies from Fisher Scientific conjugated to different fluorophores were used at a dilution of 1:400-1:600. For LSR immunofluorescence, donkey secondary antibody A488 Plus (A48269, Invitrogen) was used. Images were acquired with Leica SP8 confocal microscope. Image acquisition was done using 25x, 40x and 63x objectives. Images were processed using LAS (Leica), ImageJ (NIH) and Photoshop (Adobe) softwares.

In situ hybridization (ISH)

C57BL/6J mice of both sexes (9–14 weeks) were euthanized by cervical dislocation, brains were dissected out and cerebellum was removed. Cerebrum was mounted for coronal sectioning in NEG-50™ (Richard Allan Scientific) and snap frozen. RNAscope® Multiplex Fluorescent Reagent Kit (v.2) (Advanced Cell Diagnostics, United States) and TSA Plus reagents (Perkin Elmer) were used according to manufacturer's protocol for fresh frozen sections with minor modifications. Briefly, 14 μm coronal cryosections were fixed with 4% buffered formaldehyde (Histolab Products AB) for 25 min at 4 °C and rinsed twice with PBS. Pre-treatment was performed by dehydration using ethanol (50%, 70%, and 2x 100%) for 5 min at RT, subsequently slides were stored in 100% EtOH at -20°C for up to 1 week, or processed immediately. Sections were dried and a hydrophobic barrier was created using Immedge™ Hydrophobic Barrier Pen (Vector Laboratory, United States). Autofluorescence was quenched using a Bloxall™ blocking solution (Vector laboratories) for 10 min at RT, sections were rinsed twice with water and permeabilized for 20 min with pretreat III. After rinsing twice with PBS, 100μl of probe mix was applied to sections and they were incubated for 2h at 40°C. Fluorescence signals were developed and amplified according to manufacturer's protocol. In case samples were stained with antibodies after ISH, they were blocked 1 hour at room temperature with Serum-Free Protein Block (Dako) and incubated over night with primary antibodies (in 1x PBS), washed with 1xPBS and stained with appropriate donkey secondary antibodies (Jackson Research). Proprietary (Advanced Cell Diagnostics) probes used were: Mm-Crabp2 (583461-C3), Mm-Col12a1 (312631), Mm-Col15a1 (1092391-C2), Mm-Dpep1 (480831-C3), Mm-Dpp4 (412571C3), Mm-Fmod (479421 and 479421-C2), Mm-Lama1 (494931), Mm-Moxd1 (497531-C3), Mm-Pdgfra (518041-C1 or C2), Mm-Pecam1 (316721 and 316721-C3), Mm-Ppp1r1a (492601), Mm-Sidt1 (425471-C3), Mm-Slc7a11 (422511-C2), Mm-Slc7a14 (544781-C2), Mm-Slc22a2 (513071), Mm-Slc47a1 (513101). Primary antibodies: Goat-anti-Dpp4 (1:200, R&D Systems, AF954) and rabbit-anti-vWF (1:200, Dako, A0082).

Images were acquired with Leica SP8 confocal microscope. Image acquisitions were done using 25x and 40x objectives. Images were processed using LAS (Leica) and ImageJ (NIH) softwares.

Transmission electron microscopy (TEM)

Two three months old *C57Bl6/J* mice (one male and one female) were perfusion fixed through the heart with MORF fixative (2.5% glutaraldehyde, 1% paraformaldehyde in 0.1M PIPES buffer, pH 7.4), the brain was dissected out and postfixed in MORF at +4°C overnight. Coronal vibratome sections (200 μm) of the cerebral cortex were generated and stored in MORF until embedding in LR white. Vibratome sections were processed 10 min in 0.1M phosphate buffer, pH 7.4; 60 min in 1% osmium tetroxide in 0.1% phosphate buffer, pH 7.4; 10 min in 50% EtOH; 10 min in 70% EtOH; 10 min in 95% ETOH; 15 min in 100% EtOH; 5 min in propylene oxide; 60 min in propylene oxide:Eponate 12™ (Ted Pella); overnight in Eponate 12™; cut in smaller pieces and transferred to tightly sealed gelatin capsules filled with Eponate 12™ and incubated at 60°C for 48h to polymerize. 1 μm sections were generated and stained with Toluidine blue to identify region of interest. Finally, ultra-thin sections (60 nm) were cut on a UC7 ultramicrotome (Leica) and collected on nickel mesh grids coated with a Formvar film (Ted Pella). Sections were analyzed in a Tecnai™ G2 Spirit BioTwin at 80 kV.

Immuno-EM

A three months old *C57Bl6/J* mouse was perfusion fixed through the heart with immuno-fix (4% paraformaldehyde, 0.01% glutaraldehyde in 0.1M phosphate buffer, pH 7.4). The brain was dissected out, post-fixed in immuno-fix at 4 °C for 4h and washed in 0.1M phosphate buffer, pH 7.4. Coronal vibratome sections (400 μm) of the cerebral cortex were generated and stored in phosphate buffer. Vibratome sections were processed 10 min in 0.1M phosphate buffer, pH 7.4; 10 min in 50% EtOH; 10 min in 70% EtOH; 10 min in 95% ETOH; 15 min in 100% EtOH; 60 min in 100% EtOH:LR White (Ted Pella); overnight in pure LR White; cut in smaller pieces and transferred to tightly sealed gelatin capsules filled with LR White and incubated at 55°C for 48h to polymerize. 1 μm sections were generated and stained with Toluidine blue to find region of interest. Finally, ultra-thin sections (60 nm) were cut on a UC7 ultramicrotome (Leica) and collected on nickel mesh grids coated with a Formvar film (Ted Pella). Sections were processed 1 min in PBS; 15 min in 50 mM glycine in PBS; 30 min AURION blocking solution for Donkey gold conjugates; 3 x 5 min in 0.2% AURION BSA-C incubation and wash solution; 60 min in 5 μg/ml primary antibody goat-anti-Dpp4 (AF954, R&D Systems); 6 x 5 min in 0.2% AURION BSA-C incubation and wash solution; 90 min in secondary antibody AURION ultrasmall anti-goat (1:200); 6 x 5 min

in 0.2% AURION BSA-C incubation and wash solution; 6 x 5 min in MQ water; 25 min in AURION Silver enhancement kit; 6 x 5 min in MQ water; 5 min in 5% uranyl acetate; rinse in MQ water; 1 min in Reynolds' lead citrate; rinse in MQ water and air dried. Sections were analyzed in a Tecnai™ G2 Spirit BioTwin at 80 kV.

Traumatic brain injury (TBI)

Male C57Bl6/J (Charles River) mice (3 months old) were anesthetized with 5% isoflurane and sustained through intraperitoneal injection of ketamine and medetomidine 10μL/g (solution of 10mg/mL Ketador™ + 0.05mg/mL Domitor™) while buprenorphine (Temgesic™) (0.05 mg/kg) was administered subcutaneously to achieve analgesia. In the cranial midline, 0.10 mL of bupivacaine (Marcaine™ 0.25%) was injected subcutaneously in the scalp providing local anesthesia. Eye-gel (containing fusidic acid (Fucithalmic™)) was applied for eye-protection. Isotonic saline (NaCl 9 mg/mL) was used to rinse and clean the scalp wound throughout the experiment. Following pre-medications, the animal was placed on a heating pad (TCAT Animal Heating Plate, Bioseb, Vitrolles, France) attached to a stereotaxic frame (Model 900, Agnthos, Stockholm, Sweden). During the surgical procedure, the animal's body temperature was maintained within a normal range.

Following a midline incision, dissection through the galea and subcutaneous tissue was performed to expose the cranial bone. For precision, a surgical microscope (Wild Heerbrugg M3C Stereozoom Microscope, Leica, Wetzlar, Germany) was used. Using a surgical drill (ANSPACH EG1 High Speed System, Anspach, DePuy Synthes, Johnson & Johnson, New Brunswick, NJ, USA) with a diamond tip of 0.5 mm diameter (05D-G1, Anspach, DePuy Synthes, Johnson & Johnson, New Brunswick, NJ, USA) a rectangular craniectomy was performed measuring approximately 3 x 4 mm of the parietal bone over the right hemisphere, leaving the underlying dura mater intact. Following this step, the heating-pad and frame was placed in a commercially available controlled cortical impact (CCI) device (TBI 0310, Precision Systems and Instrumentation LLC, Lexington, KY, USA), a model of focal brain injury.[65,66] A 3-mm diameter piston was used to impact a 2 mm deep lesion in the right parietal lobe (velocity 3.5 m/s and dwell time 500 ms), an injury commonly defined as a "severe TBI" in mice.[67] The animal was then returned to the surgical set-up, the wound rinsed with NaCl, and the skin sutured using monofilament sutures (Ethicon™ 4-0, Johnson & Johnson, New Brunswick, NJ, USA). The animal was then administered atipamezole hydrochloride intraperitoneally 10μL/g (Antisedan™) and NaCl subcutaneously (1 mL) and placed on a heating pad until fully awake.

28d post-injury mice (n=3) were euthanized by cervical dislocation and brains were carefully dissected and placed in OCT (NEG -50, Fisher Scientific) for cryo-sectioning and ISH analysis. One brain was isolated 28 days after injury for TEM. Here, mice were anesthetized using avertin, perfused through the heart and post-fixed with MORF fixative, as described above, before sectioning for TEM analysis.

QUANTIFICATION AND STATISTICAL ANALYSIS

In single cell RNAseq data analysis, the FindAllMarkers function in Seurat package was used to access the statistical significance for the marker/enriched genes for each cluster, and a Wilcoxon Rank Sum test was applied to identify the differentially expressed genes between groups. The default fold change cut-off 0.25 (log) and bonferroni multiple test corrected p value = 0.05 were set as the significance cut-off. To access the statistical significance for the functional enrichment of the enriched genes, the GO analysis was performed in R software using GOstat packages (version 2.48.0) and GO.db (version 3.6.0). The statistics p value = 0.001 was set as the significance cut-off (Tables S1 and S2). The top 2000 most variable genes for each single cell dataset were identified using the vst method in FindVariableFeatures function in Seurat package (Table S3). No additional statistical methods were used to predetermine the data distribution.

To compare the average expression between different clusters, we plotted the cluster means (average over all cells) and the standard error of the mean (Figures S3–S5). The numbers of cells in each cluster are shown in the parallel individual cell expression plot (Figures S3–S5). To summarize the individual cell expression in different clusters in the embryonic mouse brain, the geom_boxplot function in R ggplot2 package (version 3.2.1) was used to produce the box plot (Figure S6). The middle line in the box shows the median, and the lower and upper hinges correspond to the first and third quartiles. The numbers of cells in each cluster are listed in Figure S6B.